

1      **Stratification Breakdown in Antarctic Coastal Polynyas, Part I: Influence of**  
2      **Physical Factors on the Destratification Timescale**

4      Yilang Xu,<sup>a,b</sup> Weifeng (Gordon) Zhang,<sup>a</sup> Ted Maksym,<sup>a</sup> Rubao Ji,<sup>c</sup> and Yun Li<sup>d</sup>

5      <sup>a</sup>*Applied Ocean Physics and Engineering Department, Woods Hole Oceanographic Institution,*  
6      *Woods Hole, Massachusetts*

7      <sup>b</sup>*MIT-WHOI Joint Program in Oceanography/Applied Ocean Science and Engineering,*  
8      *Cambridge, Massachusetts*

9      <sup>c</sup>*Biology Department, Woods Hole Oceanographic Institution, Woods Hole, Massachusetts*

10     <sup>d</sup>*School of Marine Science and Policy, University of Delaware, Lewes, Delaware*

12     *Corresponding author: Yilang Xu, yilangxu@mit.edu*

## ABSTRACT

15 This study examines the process of water-column stratification breakdown in Antarctic  
16 coastal polynyas adjacent to an ice shelf with a cavity underneath. This first part of a two-part  
17 sequence seeks to quantify the influence of offshore katabatic winds, alongshore winds, air  
18 temperature, and initial ambient stratification on the timescales of polynya destratification through  
19 combining process-oriented numerical simulations and analytical scaling. In particular, the often-  
20 neglected influence of wind-driven circulation on the lateral transport of the water formed at the  
21 polynya surface — which we call Polynya Source Water (PSW) — is systematically examined  
22 here. First, an ice-shelf/sea-ice/ocean coupled numerical model is adapted to simulate the process  
23 of PSW formation in polynyas of various configurations. The simulations highlight that i) before  
24 reaching the bottom, majority of the PSW is actually carried away from the polynya by katabatic  
25 wind-induced offshore outflow, diminishing water-column mixing in the polynya and intrusion of  
26 the PSW into the neighboring ice shelf cavity, and ii) alongshore coastal easterly winds, through  
27 inducing onshore Ekman transport, reduce offshore loss of the PSW and enhance polynya mixing  
28 and PSW intrusion into the cavity. Second, an analytical scaling of the destratification timescale  
29 is derived based on fundamental physical principles to quantitatively synthesize the influence of  
30 the physical factors, which is then verified by independent numerical sensitivity simulations. This  
31 work provides insights into the mechanisms that drive temporal and cross-polynya variations in  
32 stratification and PSW formation in Antarctic coastal polynyas, and establishes a framework for  
33 studying differences among the polynyas in the ocean.

35 **1. Introduction**

36 Polynyas, areas of persistent open water surrounded by sea ice, are ubiquitous along the  
37 coast of Antarctica (Arrigo and van Dijken 2003) and key components of the Antarctic marine  
38 system (Smith and Barber 2007). Antarctic coastal polynyas are often formed by strong offshore  
39 katabatic winds with wind speed  $\geq 25 \text{ m s}^{-1}$  (Rusciano et al. 2013). The enhanced sea ice  
40 formation and brine rejection produce saline Dense Shelf Water (DSW), which sinks in the  
41 polynya water column, causing substantial vertical mixing (Morales Maqueda et al. 2004).  
42 Deepening of the mixed layer in winter brings the nutrient-rich deep water to the surface layer,  
43 stimulating biological production in subsequent warmer seasons (Li et al. 2016). If the deepened

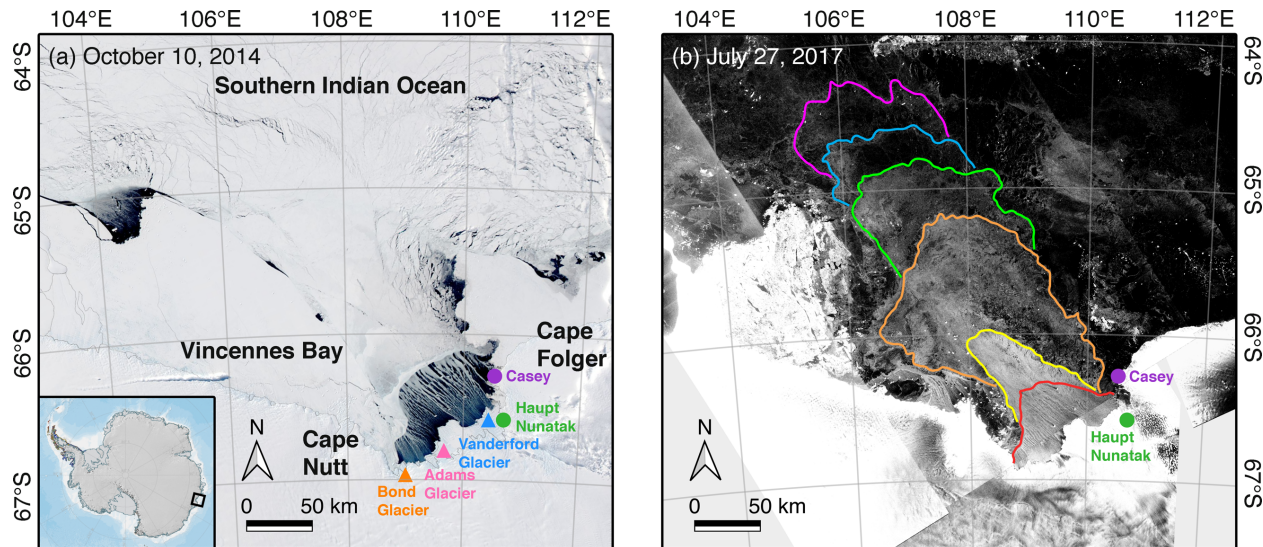
44 mixed layer reaches the bottom within the winter months, DSW could flow offshore into the  
45 abyssal ocean forming Antarctic Bottom Water (AABW) (Kitade et al. 2014; Ohshima et al. 2013).  
46 These physical and biological processes depend highly on the extent of winter mixing in the  
47 polynyas (Aoki et al. 2020; Li et al. 2016). Therefore, it is important to determine the wintertime  
48 mixing intensity and destratification timescale in the polynyas.

49 Coastal polynyas around Antarctica vary substantially in terms of their duration of opening,  
50 rate of DSW formation, mixing strength, and AABW export. For instance, AABW forms in the  
51 Cape Darnley, Mertz, and Ross Sea Polynyas (Ohshima et al. 2013; Williams et al. 2010; Jacobs  
52 et al. 1970), but not in the Bellingshausen Sea and Amundsen Sea Polynyas (Schmidtko et al. 2014;  
53 Silvano et al. 2018). This difference could result from variations in either shelf physical conditions  
54 or dense water sources. DSW formation in polynyas depends on local factors such as atmospheric  
55 forcings, sea ice productivity, and strength of ocean stratification (Ohshima et al. 2013; Silvano et  
56 al. 2018; Williams and Bindoff 2003). To evaluate the influence of these factors on polynya  
57 processes, regional models with realistic configurations are often used (e.g., Mathiot et al. 2012;  
58 Nakayama et al. 2017; Schultz et al. 2020). However, this type of model often requires special  
59 effort in resolving complex patterns of ice-shelf/ocean interactions (Nakayama et al. 2017), sea-  
60 ice dynamics (Schultz et al. 2020), and katabatic winds (Mathiot et al. 2012).

61 Idealized models have also been used to investigate the polynya DSW dispersal and  
62 impacts of physical factors on the dispersal (Årthun et al. 2013; Chapman and Gawarkiewicz 1997;  
63 Chapman 1998; 1999; Visbeck et al. 1996; Wilchinsky and Feltham 2008; Zhang and Cenedese  
64 2014). These studies often use a negative surface buoyancy flux (i.e., downward salt flux) over a  
65 fixed area to represent polynya brine rejection. They demonstrated that the density gradient  
66 between the dense water chimney and the ambient fluid creates a front, which, through thermal-  
67 wind balance, generates a geostrophic rim current around the polynya edge. Baroclinic instability  
68 of the rim current then develops into eddies, carrying dense water away from the polynya (Årthun  
69 et al. 2013). Analytical scales of the time and magnitude of dense water downslope propagation  
70 have been developed (Chapman 1998; Visbeck et al. 1996). All these idealized numerical and  
71 analytical studies were performed in the absence of winds and sea ice. They neglected the  
72 momentum exchange among the atmosphere, sea ice and ocean, and the influence of wind-driven  
73 circulation. How these factors affect the polynya dynamics remains unknown.

74 This study seeks to systematically diagnose the influence of a number of physical factors,  
 75 including winds, air temperature, initial stratification, ice tongue, and coastal geometry on the  
 76 dispersal of the water mass formed at the polynya surface, which we named Polynya Source Water  
 77 (PSW) for the purpose of this paper. Note that DSW is part of the PSW that is dense enough to  
 78 sink to the bottom, while the remaining portion is diluted on its way down by the ambient water  
 79 and gradually loses its density anomaly in the water column. The Vincennes Bay Polynya (VBP;  
 80 Fig. 1a) and Terra Nova Bay Polynya (TNBP) are used to illustrate the general pattern of polynya  
 81 circulation and guide the design of idealized models that are applicable to other polynyas on the  
 82 Antarctic coast. The VBP is used in Part I to highlight the importance of katabatic winds, while  
 83 the TNBP is used in Part II (Xu et al. 2023) to demonstrate the influence of an ice tongue and a  
 84 headland.

85



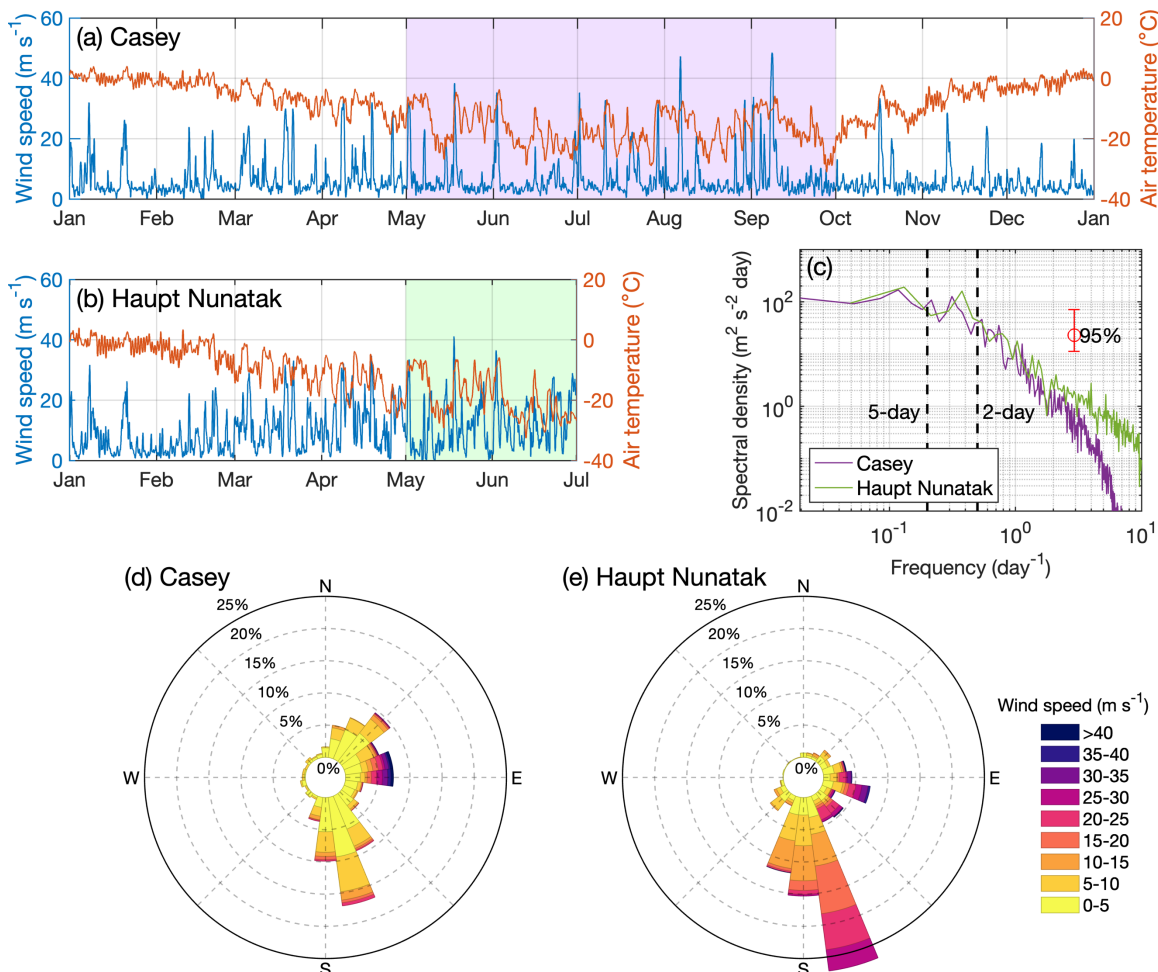
86 **Fig. 1.** (a) Terra/Aqua MODIS satellite image of the Vincennes Bay Polynya on 10 October, 2014, and  
 87 (b) Sentinel-1 SAR satellite image of the Vincennes Bay Polynya on 27 July, 2017. The triangles in (a) locate  
 88 the nearby glaciers; circles in (a) and (b) denote the locations of Casey and Haupt Nunatak weather stations;  
 89 colored lines in (b) outline the offshore boundary of the polynya and outer boundaries of the previous sea ice  
 90 plume. These images are selected to show a clear (cloud-free) pattern of the polynya surface and its offshore sea  
 91 ice plume in winter.

93

94 The VBP is located in the Indian Ocean sector of the Antarctic coast, between Cape Nutt  
 95 and Cape Folger. In winter, strong katabatic winds are channeled into the Vanderford, Adams, and  
 96 Bond Glaciers, blow offshore (northwestward), and extend beyond the Vincennes Bay (Nihashi

97 and Ohshima 2015; Parish and Bromwich 2007), forming the VBP. Data from the nearby Casey  
 98 and Haupt Nunatak weather stations (Barnes-Keoghan 2000) show intensification of winds during  
 99 2017 winter (May–September) when the air temperature frequently drops below  $-20^{\circ}\text{C}$  (Fig. 2a-  
 100 b). The katabatic winds are mainly offshore (Fig. 2d-e), particularly at the Haupt Nunatak station,  
 101 close to the center of the polynya (Fig. 1). Spectra of the wind speed show strong oscillations in  
 102 the period band of 2-5 days (Fig. 2c). Besides the offshore winds, alongshore easterly winds are  
 103 also present (Fig. 2d). These conditions of offshore and coastal easterly winds are common to  
 104 Antarctic coastal polynyas (e.g., Mathiot et al. 2010; Nihashi and Ohshima 2015).

105



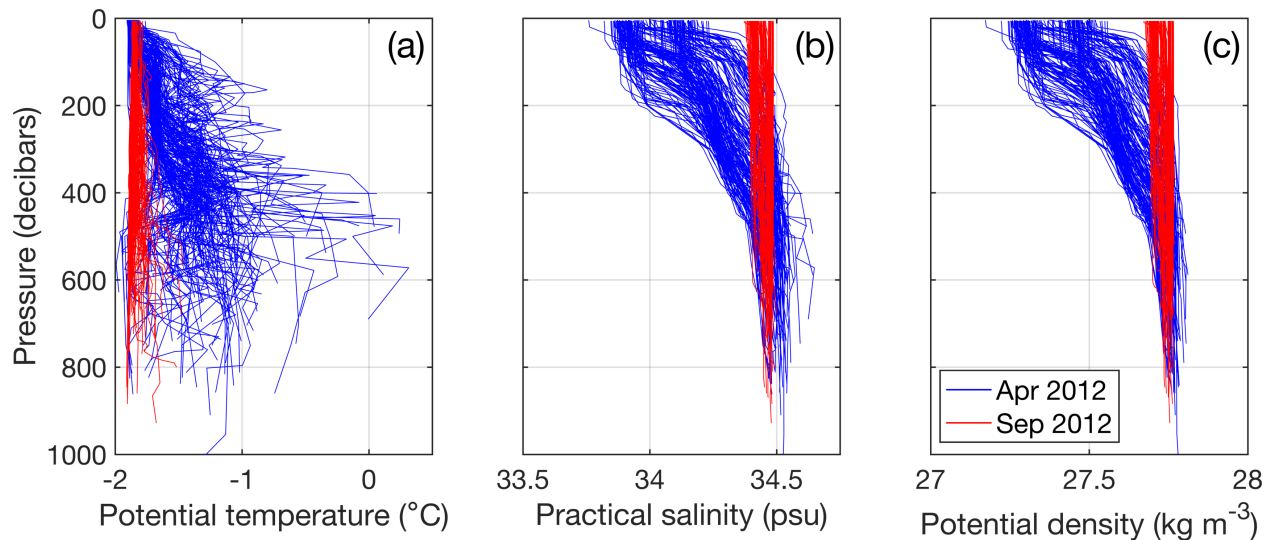
106

107 **Fig. 2.** (a-b) Wind speed and air temperature measured at the Casey and Haupt Nunatak weather stations  
 108 in 2017; (c) spectral density of the measured wind speed; (d-e) wind rose plots of the wind speed and the direction  
 109 it comes from in the winter months (May–September). Note that the Haupt Nunatak station is closer to the center  
 110 of the polynya, but no data is available there for the second half of 2017. The purple and green shades in (a) and  
 111 (b) highlight the austral winter months; the error bar in (c) indicates the 95% confidence interval; dashed lines  
 112 in (c) denote frequencies corresponding to wind periods of 2 and 5 days.

113

114 Wintertime katabatic winds at the VBP are accompanied by enhanced offshore sea ice  
 115 export, as indicated by the offshore-flowing sea ice plume in the Sentinel-1 SAR satellite image  
 116 (Fig. 1b). Similar sea ice plumes have been reported in other Antarctic coastal polynyas, including  
 117 the Ross Sea Polynya, and the bright-dark bands in the plumes represent episodic export of sea ice  
 118 induced by katabatic wind events (Dai et al. 2020). Overall, the VBP has a medium sea ice  
 119 production rate ( $73.3 \pm 9.9 \text{ km}^3$  per year) among the major Antarctic coastal polynyas (30 to 400  
 120  $\text{km}^3$  per year; Tamura et al. 2008). It forms DSW that flows offshore supplying the AABW (Kitade  
 121 et al. 2014). The process of DSW formation and water column destratification in the VBP is  
 122 captured by temperature and salinity profiles from instrumented elephant seals (Roquet et al. 2014;  
 123 Roquet et al. 2021). For example, during April 2012 (early winter), the water column in the VBP  
 124 is stratified (Fig. 3). The mean salinity difference between the surface and bottom layers is  $\sim 0.4$   
 125 psu and the mean density difference is  $\sim 0.3 \text{ kg m}^{-3}$ . Note that temperature changes in the region  
 126 have negligible influence on density, and salinity changes completely dominate the density  
 127 variation. By the end of the winter (September 2012), the polynya water column is completely  
 128 mixed. It thus took less than 5 months to break down the water column stratification in this case.

129



130

131 **Fig. 3.** (a) Potential temperature, (b) practical salinity and (c) potential density profiles recorded by  
 132 instrumented elephant seals in the Vincennes Bay Polynya between 109-110°E, 66-67°S in April (early winter)  
 133 and September (late winter), 2012.

134

135 Here we hypothesize that the strength of wintertime vertical mixing and the time required  
136 to break down the water column stratification in coastal polynyas are affected by polynya  
137 circulation. Both winds and coastal geometry (e.g., ice tongues and headlands) can modify three-  
138 dimensional polynya flows and potentially affect the lateral dispersal of the water mass formed by  
139 buoyancy loss at the polynya surface. Therefore, the process of polynya mixing is likely a three-  
140 dimensional process, rather than a one-dimensional (vertical) process that is often assumed by  
141 previous studies. Focusing on the impact of the wind-driven circulation on polynya mixing, this  
142 Part I study uses an ice-shelf/sea-ice/ocean coupled numerical model to simulate idealized  
143 Antarctic coastal polynyas and investigate the water-column destratification timescale. The impact  
144 of polynya circulation induced by complex coastal geometry will be studied in Part II.

145

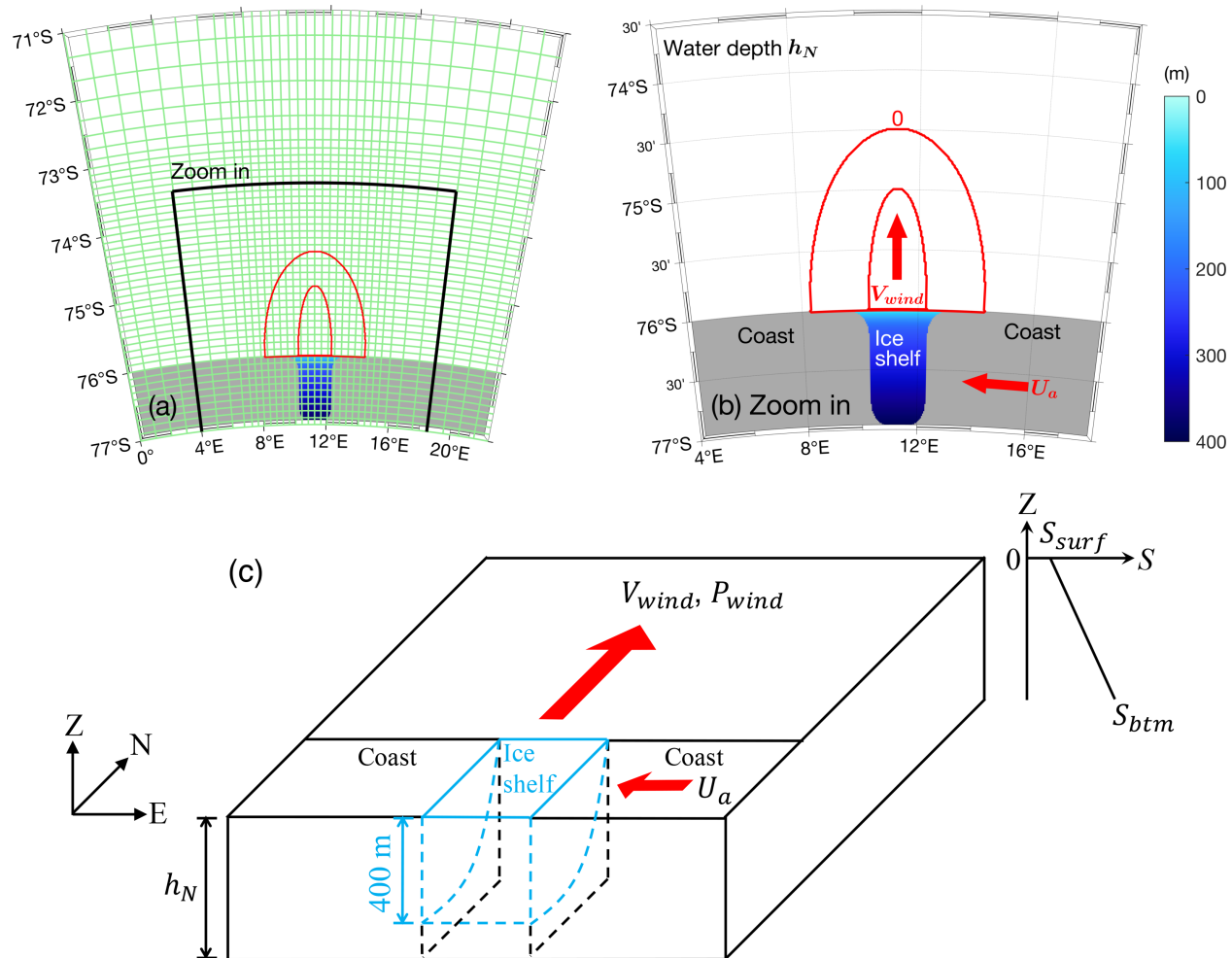
## 146 **2. Numerical Model**

### 147 *a. Model Setup*

148 The MIT General Circulation Model (MITgcm; Marshall et al. 1997) with coupled ice shelf,  
149 sea ice (Losch 2008; Losch et al. 2010) and ocean modules is used here. MITgcm has been used  
150 in various Antarctic coastal studies (Nakayama et al. 2017; Nakayama et al. 2019; Schultz et al.  
151 2020). We use an idealized setup to capture fundamental processes in a wide range of Antarctic  
152 coastal polynyas. The model uses a spherical polar coordinate and covers a region of  $22.5^{\circ}$  in  
153 longitude ( $0$ – $22.5^{\circ}$ E) and  $6^{\circ}$  in latitude ( $77$ – $71^{\circ}$ S) with a uniform water depth  $h_N$  (Fig. 4). Note  
154 that the absolute values of the coordinates in this process-oriented idealized study are used for  
155 convenience, similar to previous studies (e.g., Årthun et al. 2013; Wilchinsky and Feltham 2008),  
156 and the model result does not change with coordinates within the range of Antarctica coastal  
157 polynyas (Section 4). The southern boundary of the domain is on the land, which is incised by an  
158 ice shelf (see below), while the other three boundaries are open in the ocean. The horizontal grid  
159 spacing is  $\sim 1$  km in the central study area and gradually increases toward the open boundaries  
160 (Fig. 4a). Because the Rossby deformation radius in the Antarctic coastal region is  $\sim 5$  km, a  
161 horizontal grid spacing of 1 km or less is required to resolve baroclinic eddies associated with the  
162 PSW dispersal (Årthun et al. 2013). The model vertical grid is uniformly spaced with a layer  
163 thickness of 10 m. Note that at  $\sim 1$  km horizontal resolution, modeled characteristics of PSW  
164 transport are similar between hydrostatic and nonhydrostatic simulations (Årthun et al. 2013). This

165 is consistent with the fact that the nonhydrostatic convection induced by the brine rejection occurs  
 166 over a much smaller horizontal scale and thus cannot be explicitly resolved by any models at this  
 167 resolution. Hence, the hydrostatic approximation is used here for faster computations, and the  
 168 implication will be discussed in Section 5.

169



170  
 171 **Fig. 4.** (a) An aerial view of the model domain and grid and (b) a zoomed-in view of the region marked  
 172 by black lines in (a). Green lines in (a) depict every 10 horizontal grid cells; the grey regions in (a) and (b)  
 173 indicate land; the filled color shows the vertical position of the interface between the ice shelf and ocean, i.e.,  
 174 thickness of the ice shelf; red ellipses outline regions of the offshore katabatic wind  $V_{wind}$  and its inner region  
 175 of maximum speed; red arrows in (b) indicate the directions of  $V_{wind}$  and the alongshore easterly winds,  $U_a$ , in  
 176 Run B2; (c) a three-dimensional schematic illustration of the model setup and the initial salinity profile.  
 177

178 A rectangular ice shelf, located between  $10.3^{\circ}\text{E}$  and  $12.3^{\circ}\text{E}$ ,  $77^{\circ}\text{S}$  and  $76^{\circ}\text{S}$ , is sandwiched  
 179 by land on both sides, and its offshore end aligns with the ambient coastline. The cross-sectional  
 180 shape of the ice shelf follows those in Årthun et al. (2013) and Losch (2008) with ice thickness  
 181 decreasing gradually northward from the maximum value of 400 m on the southern end to 0 on  
 182 the northern edge. The vertical profile of the ice shelf front is smoothed to improve numerical  
 183 stability and its wedge shape forms a cavity underneath. The katabatic winds blow northward off  
 184 the ice shelf front. To mimic the katabatic wind patterns in the Antarctic Mesoscale Prediction  
 185 System as analyzed by Guest (2021a) and Wenta and Cassano (2020), the wind field specified in  
 186 this study has a half-elliptic shape with the highest speed in the central region between  $10.3^{\circ}$  and  
 187  $12.3^{\circ}\text{E}$  and  $76^{\circ}\text{S}$  and  $75^{\circ}\text{S}$ , and it linearly decays outward to 0 in a region of  $\sim 55$  km wide (Fig.  
 188 4b). Based on the winds measured near coastal polynyas around Antarctica (e.g., Adolfs and  
 189 Wendler 1995; Knuth and Cassano 2011; Wendler et al. 1997) and the wind data presented in Fig.  
 190 2, the katabatic wind speed at 10 m height,  $V_{wind}$ , is assumed to oscillate with time  $t$  following the  
 191 form,

$$V_{wind} = V_a \left[ 1 - \cos \frac{2\pi t}{P_{wind}} \right], \quad (1)$$

192 where  $P_{wind}$  is the wind oscillation period and  $V_a$  is the time-averaged wind speed. Within an  
 193 oscillation period,  $V_{wind}$  varies between 0 and  $2V_a$ .

194 To include the effect of coastal easterly winds that are ubiquitous along the Antarctic coast,  
 195 in some of the simulations, westward winds with speed  $U_a$  are prescribed over most of the domain.  
 196  $U_a$  linearly decreases to 0 within a  $\sim 80$ – $110$  km wide ramping zone adjacent to the open boundaries.  
 197 For simplicity, only steady alongshore wind speed is considered here. Additional simulations with  
 198 oscillating alongshore winds suggest that oscillations in alongshore winds do not change the  
 199 general dispersal pattern of the water mass formed at the polynya surface (not shown).

200 The sea ice module (Losch et al. 2010) used is based on the viscous-plastic dynamic-  
 201 thermodynamic sea ice model proposed by Zhang and Hibler (1997). Sea ice parameters are  
 202 adapted from the LLC4320 simulation (Rocha et al. 2016) with the following modifications. The  
 203 sea ice is discretized into 7 thickness categories, and the subgrid-scale ice thickness distribution  
 204 scheme is used, which follows the probability density function proposed by Thorndike et al. (1975)  
 205 and the participation and ridging function in Lipscomb et al. (2007). Sea ice strength changes with

206 its concentration and thickness, and is parameterized following Hibler (1979). Table 1 shows  
 207 values of the sea ice parameters in MITgcm used in this study. To represent early-winter conditions,  
 208 the model is initialized with sea ice concentration of 1 (100% of the grid area) and thickness of  
 209 0.5 m over the entire domain. To avoid boundary condition issues, sea ice concentration and  
 210 thickness are set to 0 on all open boundaries. Note that the general pattern of modeled polynyas in  
 211 the middle of the domain is not sensitive to the sea ice boundary condition. The ice shelf module  
 212 implemented by Losch (2008) is used to parameterize basal melting under the ice shelf. It uses a  
 213 three-equation system with a linear turbulent flux formulation (Hellmer and Olbers 1989; Jenkins  
 214 et al. 2001) to simulate the melting/refreezing-induced mass and heat fluxes across the ice shelf  
 215 and ocean interface.

216

Name	Description	Value
SEAICE_dryIceAlb	Winter sea ice albedo	0.8509
SEAICE_wetIceAlb	Summer sea ice albedo	0.7284
SEAICE_drySnowAlb	Dry snow albedo	0.7754
SEAICE_wetSnowAlb	Wet snow albedo	0.7753
SEAICE_drag	Non-dimensional air-ice drag coefficient	0.002
SEAICE_waterDrag	Non-dimensional water-ice drag coefficient	0.0055
HO	Demarcation ice thickness	0.2 m

217 **Table 1.** Main sea ice parameters in MITgcm and their values used in this study.

218

219 To simulate the dispersal of all water mass formed by the buoyancy loss at the polynya  
 220 surface, a passive tracer is continuously injected into the polynya surface. Following the literature  
 221 (e.g., Ding et al. 2020; Parmiggiani 2006), the polynya surface in the model is defined as the coastal  
 222 area within the region of 8–14.5°E and 76–75.5°S where sea ice concentration is <70% (leads  
 223 farther offshore are excluded). At every time step, the polynya region is recomputed according to  
 224 the modeled sea ice concentration, and surface concentration of the passive tracer in the polynya

225 region is set to 1. Subject to advection, mixing and ice shelf meltwater dilution, the passive tracer  
226 spreads out vertically and horizontally, manifesting spreading of the PSW, including the DSW that  
227 sinks down to the bottom and the portion that loses its density anomaly and being carried away in  
228 the middle of the water column.

229 The nonlocal K-Profile Parameterization (KPP; Large et al. 1994) and the Smagorinsky  
230 (1963) scheme are used to simulate vertical and horizontal mixing, respectively. The minimum  
231 vertical viscosity is set to  $10^{-7} \text{ m}^2 \text{ s}^{-1}$ . The KPP background diffusivity is  $5 \times 10^{-7} \text{ m}^2 \text{ s}^{-1}$ , as  
232 suggested by Nguyen et al. (2011). The KPP scheme computes vertical mixing coefficients in the  
233 boundary layers and the interior through parameterizing the impacts of surface forcing, shear  
234 instability, internal wave activity, and static instability (Large et al. 1994). Note that model results  
235 are not sensitive to the static instability parameterization as test simulations with the static  
236 instability factor altered by 2 orders of magnitude show negligible differences in modeled  
237 destratification timescales. The third-order direct-space-time flux limiter advection scheme is  
238 applied to salinity, temperature and passive tracer. The coastal and ice shelf boundaries are free-  
239 slip, and frictional boundary condition with a quadratic drag coefficient of  $2.5 \times 10^{-3}$  is applied  
240 to the ocean bottom and the base of the ice shelf. The Orlanski radiation condition (Orlanski 1976)  
241 with preserved model volume is imposed on the lateral open boundaries for ocean temperature,  
242 salinity, and velocity.

243 For the first two base runs (hereinafter referred to as Run B1 and B2), the ocean is  
244 initialized with a near-freezing temperature of  $-1.8 \text{ }^{\circ}\text{C}$  everywhere, and a linear salinity profile of  
245 34 to 34.25 psu from the surface to the bottom (at 500 m), both representative of the hydrographic  
246 conditions in Antarctic coastal polynyas, such as the VBP (Fig. 3) and TNBP (Le Bel et al.  
247 2021; Rusciano et al. 2013). The corresponding buoyancy frequency  $N$  equals  $0.002 \text{ s}^{-1}$ . Because  
248 density variation induced by typical temperature changes in the polynyas is negligible compared  
249 to that induced by salinity changes (e.g., Ohshima et al. 2022), using an initially uniform near-  
250 freezing temperature in the model does not affect the model dynamics. Meteorological conditions  
251 typical to wintertime katabatic wind events in Antarctic coastal polynyas (Guest 2021a; 2021b)  
252 with constant downward longwave radiation of  $200 \text{ W m}^{-2}$ , specific humidity at 2 m height of  
253  $5 \times 10^{-4}$ , and air temperature at 2 m height of  $T_a = -20 \text{ }^{\circ}\text{C}$  are used. The mean offshore wind  
254 speed in Equation (1) is set as  $V_a = 20 \text{ m s}^{-1}$  with  $P_{wind} = 2 \text{ days}$ , representative of the

255 wintertime winds measured at the VBP (Fig. 2). Applying these conditions in the model produces  
256 a pattern of heat fluxes qualitatively similar to that observed in the TNBP (see Part II). In Run B1,  
257 no alongshore wind is applied, i.e.,  $U_a = 0$ , while in Run B2 steady coastal easterly wind of  $U_a =$   
258  $10 \text{ m s}^{-1}$  is applied. All simulations are integrated for 200 days.

259 To validate results of the analytical scaling, two groups of sensitivity simulations, G1 and  
260 G2, are carried out (Table 2). G1 has 6 sensitivity sets (G1-Vwind, G1-Uwind, G1-Tair, G1-Nini,  
261 G1-Hdepth, and G1-Pwind) designed around Run B1 and B2, corresponding to 6 sensitivity  
262 parameters: mean speed of the offshore winds  $V_a$ , alongshore wind speed  $U_a$ , air temperature  $T_a$ ,  
263 initial stratification  $N$ , water depth  $h_N$ , and wind-oscillation period  $P_{wind}$ . Each of the sensitivity  
264 sets consists of a number of simulations with the value of only one target parameter being altered.  
265 All other parameters are kept the same as the control values used in B1 and B2 (numbers in bold  
266 in Table 2). Note that the value of  $N$  is modified by changing the initial bottom salinity  $S_{btm}$ , while  
267 keeping surface salinity,  $S_{surf} = 34 \text{ psu}$ , fixed. Ranges of the parameter values are chosen to  
268 represent typical conditions of Antarctic coastal regions. For instance, when  $h_N = 500 \text{ m}$ ,  $S_{btm}$   
269 varies between 34 and 34.5 psu, which gives the bottom-to-surface salinity difference ( $S_{btm} -$   
270  $S_{surf}$ ) of 0–0.5 psu, consistent with observations at the VBP (Fig. 3b). Note that when the water  
271 depth  $h_N$  increases,  $S_{btm}$  increases to keep  $N = 0.002 \text{ s}^{-1}$  in the entire water column, as in Run  
272 B1 and B2. The maximum offshore wind speed  $2V_a$  varies between 25 and  $55 \text{ m s}^{-1}$ , consistent  
273 with katabatic wind speed (Rusciano et al. 2013).

274 The second group of sensitivity simulations G2, is for *independent* validation of the scaling  
275 (see below). Each simulation set in G2 differs from the corresponding set in G1 by one parameter.  
276 That is, in each G2 simulation, two parameters have values altered from those in the base run. For  
277 instance, in the G2-Vwind set, besides altering the value of  $V_a$ ,  $T_a$  is set at  $-30^\circ\text{C}$ , differing from  
278  $-20^\circ\text{C}$  in both the base run and the G1-Vwind set. Meanwhile, besides having G2-Pwind with  
279  $V_a = 15 \text{ m s}^{-1}$ , an extra set of simulations, G2-Pwindx with  $V_a = 25 \text{ m s}^{-1}$ , is added to examine  
280 the dependence on the oscillation of winds stronger than that in the base run with  $V_a = 20 \text{ m s}^{-1}$ .

281 Altogether, 63 simulations, categorized into 13 sets, are presented in this Part I study. Two  
282 sensitivity sets in G1, namely, G1-Vwind and G1-Uwind, are used to determine values of the  
283 coefficients in the analytically scaled formula through least squares fitting. They are referred to as

284 *calibration* sets. The other 11 sets are referred to as *validation* sets, as the simulations within are  
 285 independent of the analytical scaling, and they are used to validate the scaled formula.

286

Sensitivity simulation set	$V_a$ (m s $^{-1}$ )	$U_a$ (m s $^{-1}$ )	$T_a$ (°C)	$S_{btm}$ (psu)	$h_N$ (m)	$P_{wind}$ (days)
G1-Vwind*	<b>[12.5, 27.5]</b> <sup>+</sup>	0	-20	34.25	500	2
G2-Vwind <sup>§</sup>	<b>[12.5, 27.5]</b>	0	<b>-30</b>	34.25	500	2
G1-Uwind*	20	<b>[0, 15]</b>	-20	34.25	500	2
G2-Uwind <sup>§</sup>	20	<b>[0, 15]</b>	<b>-30</b>	34.25	500	2
G1-Tair <sup>§</sup>	20	0	<b>[-40, -10]</b>	34.25	500	2
G2-Tair <sup>§</sup>	<b>15</b>	0	<b>[-40, -10]</b>	34.25	500	2
G1-Nini <sup>§</sup>	20	10	-20	<b>[34, 34.5]</b>	500	2
G2-Nini <sup>§</sup>	20	<b>15</b>	-20	<b>[34, 34.5]</b>	500	2
G1-Hdepth <sup>§</sup>	20	10	-20	[34.25, 34.4] (maintain $N = 0.002 \text{ s}^{-1}$ )	<b>[500, 800]</b>	2
G2-Hdepth <sup>§</sup>	20	<b>15</b>	-20	[34.25, 34.4] (maintain $N = 0.002 \text{ s}^{-1}$ )	<b>[500, 800]</b>	2
G1-Pwind <sup>§</sup>	20	0	-20	34.25	500	<b>[0.5, 5]</b>
G2-Pwind <sup>§</sup>	<b>15</b>	0	-20	34.25	500	<b>[0.5, 5]</b>
G2-Pwindx <sup>§</sup>	<b>25</b>	0	-20	34.25	500	<b>[0.5, 5]</b>

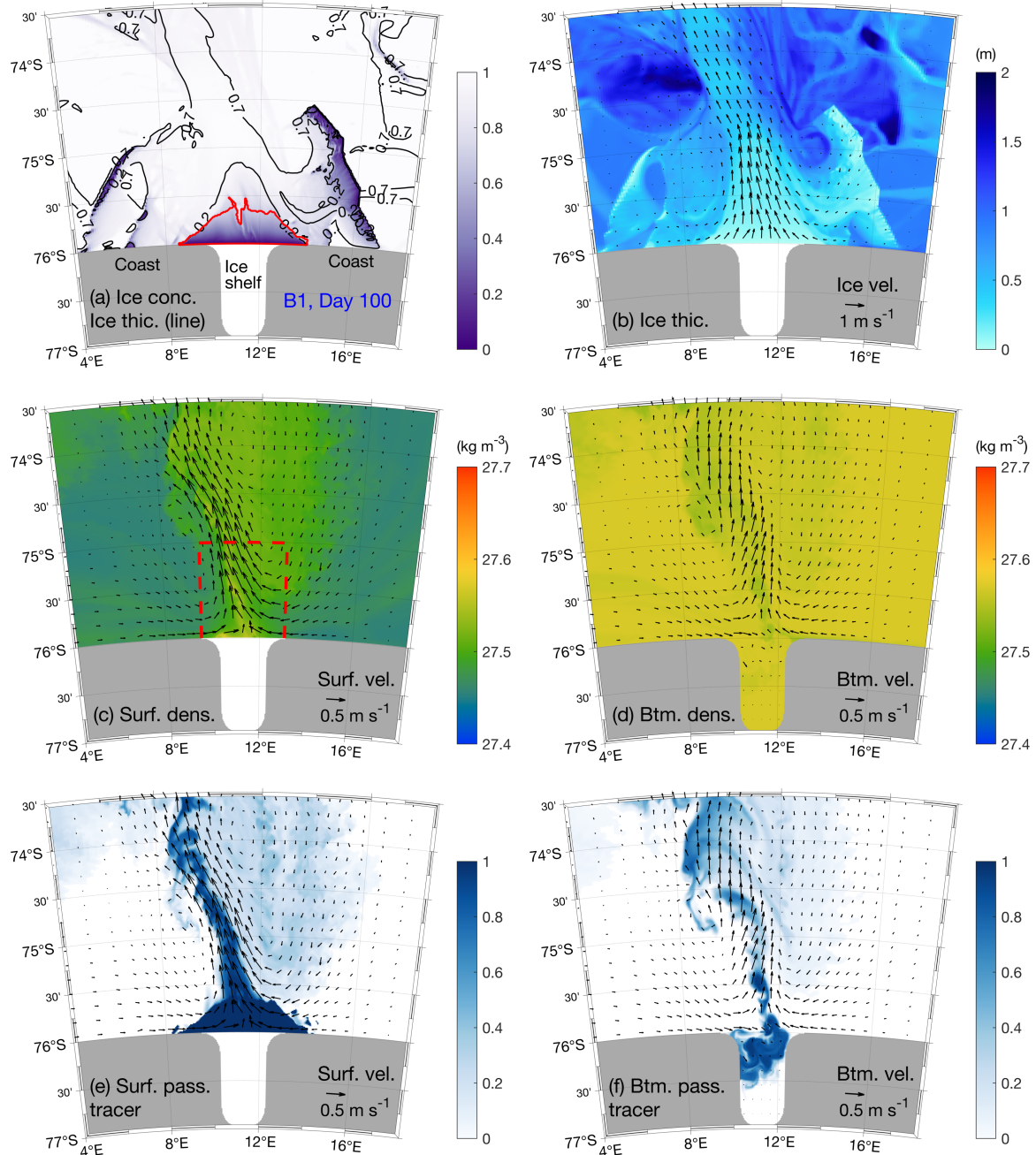
287 \* Calibration set

288 <sup>§</sup> Validation set

289 <sup>+</sup> Bracket denotes the range of the parameter values.

290 **Table 2.** Sensitivity simulations and the corresponding parameter values. The altered values of the  
 291 parameters are shown in bold.

292



293

294 **Fig. 5.** Snapshots of model fields on Day 100 from Run B1: (a) sea ice concentration (color) and  
 295 thickness (black contours in meters); (b) sea ice thickness (color) and sea ice velocity (arrows); (c-d) potential  
 296 density (color) and velocity (arrows) at the (c) surface and (d) bottom; (e-f) concentration of passive tracer (color)  
 297 originating from the polynya surface and velocity (arrows) at the (e) surface and (f) bottom. The red line in (a)  
 298 outlines the coastal polynya on Day 100; the red dashed box in (c) indicates the region where modeled fields are  
 299 averaged zonally and shown in Fig. 7.

300

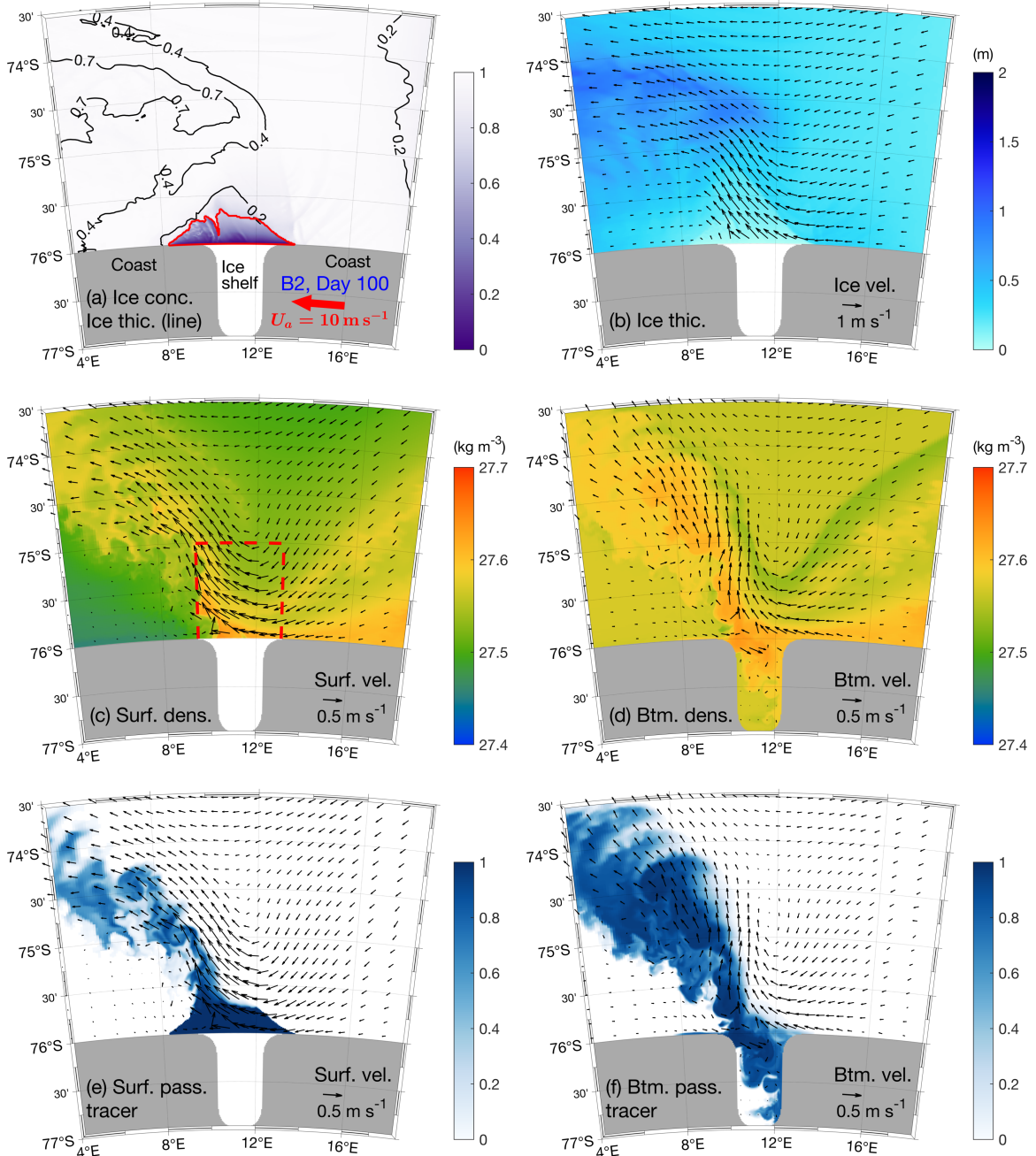


**Fig. 6.** Snapshots of model fields on Day 100 from Run B2: (a) sea ice concentration (color) and thickness (black contours in meters); (b) sea ice thickness (color) and sea ice velocity (arrows); (c-d) potential density (color) and velocity (arrows) at the (c) surface and (d) bottom; (e-f) concentration of passive tracer (color) originating from the polynya surface and velocity (arrows) at the (e) surface and (f) bottom. The red line in (a) outlines the coastal polynya on Day 100; the red dashed box in (c) indicates the region where modeled fields are averaged zonally and shown in Fig. 7.

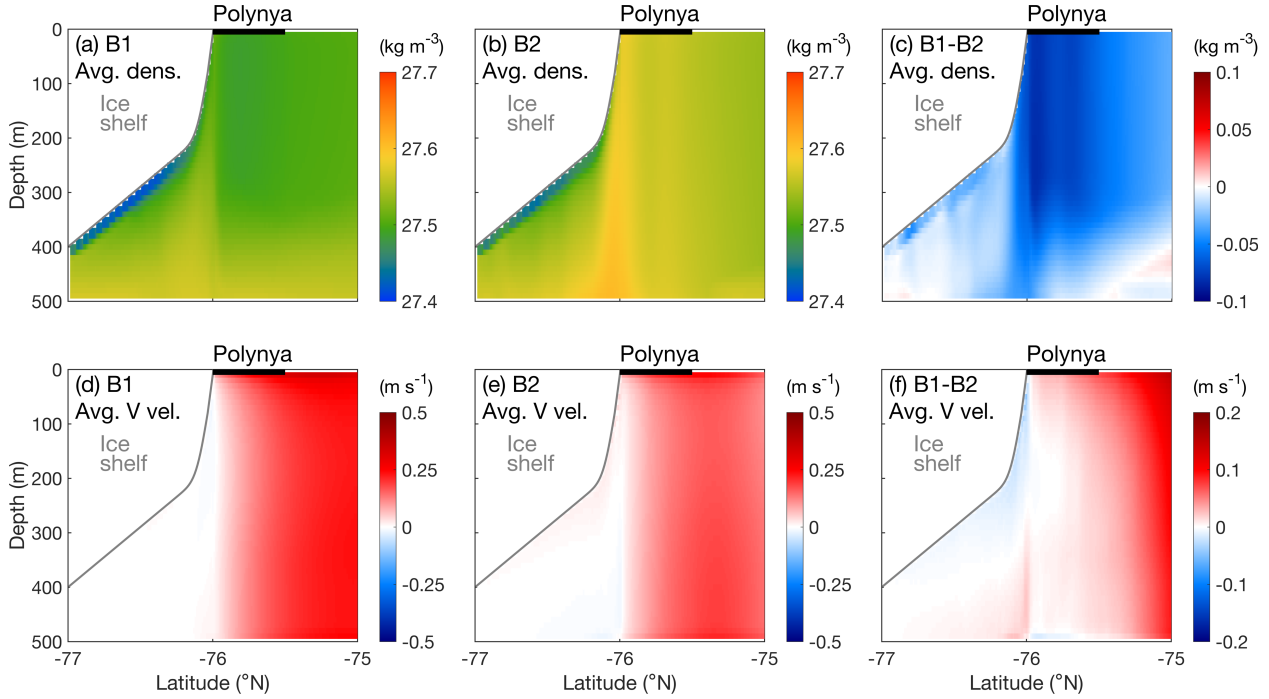
309 *b. General Pattern of Modeled Polynyas*

310 Snapshots of sea ice concentration and thickness, potential density, and passive tracer  
311 concentration on model Day 100 in both Run B1 and B2 show a coastal polynya forming at the  
312 center of the wind field (Figs. 5-6). In both simulations, as the winds push the sea ice northwards,  
313 sea ice thickness gradually increases offshore, constraining further expansion of the polynya. A  
314 strong offshore ocean current is formed. At the ocean surface, density increases not only within  
315 the polynya, but also in the offshore regions. As indicated by the passive tracer field, PSW formed  
316 at the polynya surface is carried away from the polynya by the wind-driven offshore outflow over  
317 the water column, as indicated by the surface and bottom distribution. Meanwhile, some of the  
318 PSW sinks down to the bottom layer of the polynya water column and flows into the ice shelf  
319 cavity to the south of the polynya (Figs. 5f and 6f).

320 Runs B1 and B2 also show prominent differences. In B1, the sea ice and ocean fields are  
321 nearly symmetric between the east and west with a slightly westward shift due to the Coriolis effect  
322 (Fig. 5b-d). In contrast, in B2, a strong westward veering is observed in the sea ice and surface  
323 ocean velocity fields (Fig. 6b-d). The maximum bottom density is higher in B2 than B1 (Figs. 5d  
324 and 6d). Meanwhile, more PSW has penetrated to the polynya bottom and entered the ice shelf  
325 cavity in B2 (Fig. 6f) than B1 (Fig. 5f), indicating faster sinking of PSW in the polynya in B2.

326 The major difference between circulations in B1 and B2 is that the alongshore winds in B2  
327 drive onshore Ekman transport (Ekman 1905). This is illustrated by differences in cross-shore  
328 vertical profiles of potential density and offshore velocity in the simulations (Fig. 7). The model  
329 fields here are temporally averaged over Day 90–100 and zonally averaged over the polynya region  
330 (9.5–13°E) to eliminate high-frequency and small-scale variations. The comparison shows that  
331 Run B2 produces higher density beneath the polynya surface (Fig. 7c) and weaker offshore  
332 velocity in the surface 150 m of the polynya water column (Fig. 7f). These are consistent with  
333 onshore Ekman transport generated by the coastal easterly winds suppressing the offshore current  
334 and diminishing offshore transport of the PSW. Note that Davis and McNider (1997) examined  
335 onshore Ekman transport of offshore water induced by alongshore easterly winds, but they did not  
336 consider the impact of Ekman dynamics on the PSW circulation. It will be quantified in this study.

337



338

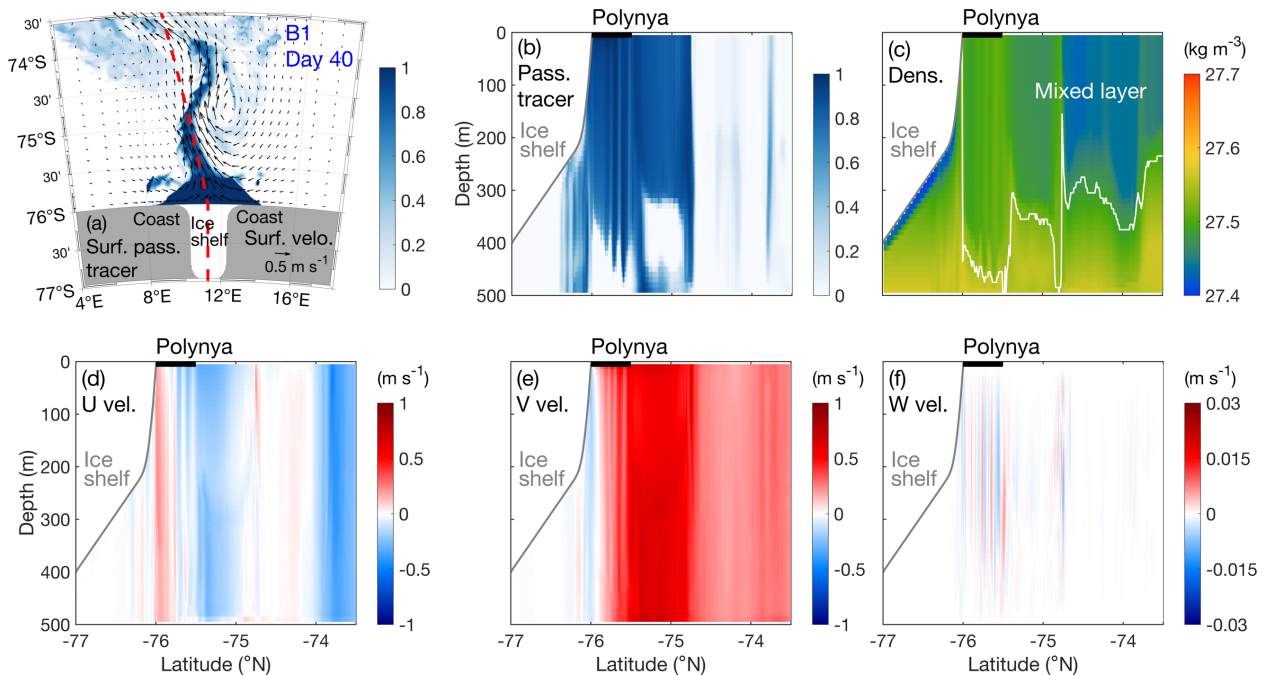
339 **Fig. 7.** Cross-shore sections of (top) potential density and (bottom) offshore velocity from Run (left) B1  
 340 and (middle) B2, and (right) their differences. The plotted fields are temporally averaged over Day 90-100 and  
 341 zonally averaged within the area delineated by the red dashed lines in Figs. 5c and 6c. The black bars on the top  
 342 of the panels highlight the polynya region.

343

344 Snapshots of the model fields along the trajectories of the PSW outflow (red dashed lines  
 345 in Figs. 8a and 9a) on Day 40 in both Runs B1 and B2 show that the wind-driven offshore flow is  
 346 largely barotropic (Figs. 8d-e and 9d-e) and that the PSW passive tracer occupies much of the  
 347 water column even offshore of the polynya (Figs. 8b and 9b). The offshore outflow thus carries  
 348 much of the PSW directly offshore before it can reach the bottom. Quantification of the modeled  
 349 passive tracer indicated that, by Day 100, 93% of the PSW is transported offshore of the polynya  
 350 in Run B1, and the rest sinks down locally in the polynya region and flows under the ice shelf.  
 351 Because the onshore Ekman transport driven by the coastal easterly winds in B2 reduces the  
 352 offshore current in the top 150 m, it suppresses offshore transport of the PSW and allows more  
 353 PSW to remain in the polynya region. By Day 100 only 85% of the polynya PSW is transported  
 354 offshore of the polynya in B2. Therefore, more PSW is able to stay in the polynya and sink down  
 355 to the polynya bottom. This is consistent with B2 having i) stronger polynya convection, as  
 356 indicated by a higher magnitude of the vertical velocity in the polynya region (Fig. 9f), ii) more  
 357 PSW passive tracer in the polynya bottom layer (Fig. 9b), iii) deeper surface mixed layer (Fig. 9c),

358 and iv) more PSW flowing into the ice shelf cavity than in B1 (Figs. 5f and 6f). Following other  
 359 studies of the high-latitude environment (e.g., Dong et al. 2008; Kusahara et al. 2017; Meehl, et al.  
 360 2019), the surface mixed layer depth (MLD) is defined as the depth where the potential density  
 361 differs from the surface density by a threshold  $\Delta\rho_{MLD} = 0.05 \text{ kg m}^{-3}$ . Note that this choice of the  
 362 density difference threshold affects values of the modeled destratification timescale, but not the  
 363 diagnosis of the dynamical influence of the factors on the timescale or the conclusion of this study.

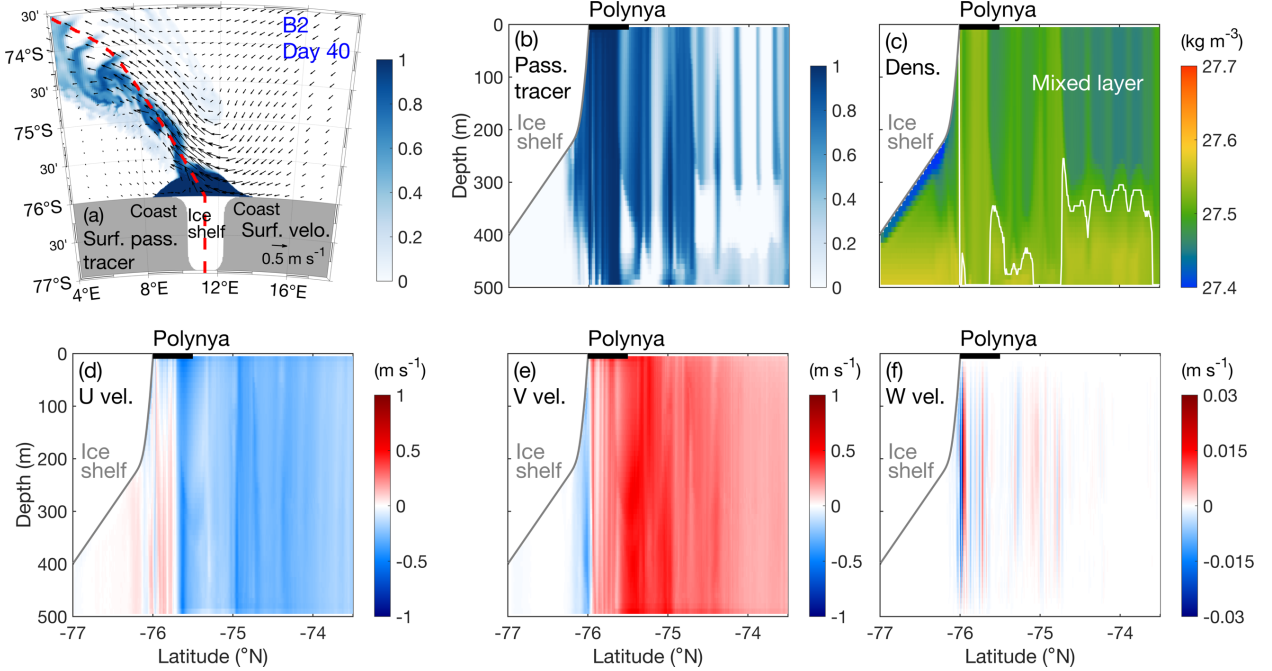
364



365

366 **Fig. 8.** Snapshots of model fields on Day 40 from Run B1: (a) surface concentration of PSW passive  
 367 tracer (color) and surface velocity (arrow); (b-f) cross-shore sections of (b) passive tracer, (c) potential density  
 368 and surface mixed layer depth (white line), (d) zonal velocity, (e) meridional velocity, and (f) vertical velocity  
 369 along the red dashed line in (a). The black bars in (b-f) highlight the polynya region.

370



371

372 **Fig. 9.** Snapshots of model fields on Day 40 from Run B2: (a) surface concentration of PSW passive  
 373 tracer (color) and surface velocity (arrow); (b-f) cross-shore sections of (b) passive tracer, (c) potential density  
 374 and surface mixed layer depth, (d) zonal velocity, (e) meridional velocity, and (f) vertical velocity along the red  
 375 dashed line in (a). The black bars in (b-f) highlight the polynya region.

376

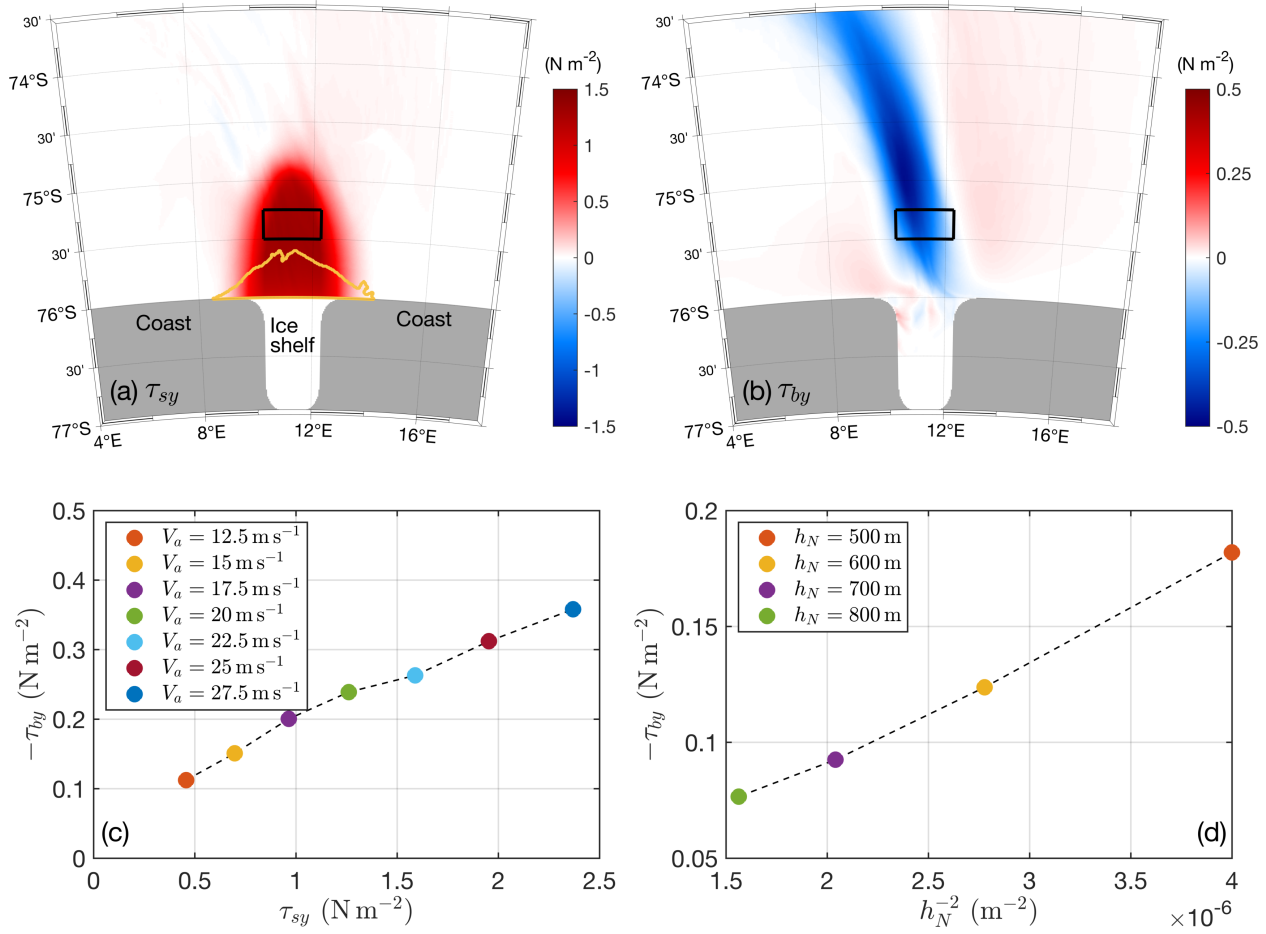
377 The modeled horizontal velocities in the ocean in both B1 and B2 being largely barotropic  
 378 over the 500 m deep water column is intriguing. It suggests that, despite the great depth, the  
 379 influence of the ocean surface stress is able to penetrate through the entire water column reaching  
 380 the bottom. To confirm that, we examine the vertically integrated cross-shore momentum balance,  
 381 which shows that a non-negligible portion of the surface stress,  $\tau_{sy}$ , is balanced by the bottom  
 382 stress,  $\tau_{by}$ . Particularly, in Run B1, the mean  $\tau_{sy}$  in a box to the immediate north of the polynya  
 383 on Days 90 to 100 is  $\sim 1.3 \text{ N m}^{-2}$ , and the mean  $\tau_{by}$  in the same region and time window is  $\sim 0.22$   
 384  $\text{N m}^{-2}$  (Fig. 10c). The sensitivity simulations (G1-Vwind) of different offshore wind strength,  $V_a$ ,  
 385 show that  $\tau_{by}$  increases almost linearly with  $\tau_{sy}$  (Fig. 10c), confirming that the imposed katabatic  
 386 winds affect the entire water column. The model also shows that the rest of the surface stress is  
 387 largely balanced by pressure gradient forces associated with sea level tilt and horizontal density  
 388 gradient. Neglecting the advection, horizontal diffusion, and Coriolis terms, the depth-integrated  
 389 cross-shore momentum balance in a steady state can be approximated as,

$$\tau_{by} \approx \tau_{sy} - \frac{g}{2} \frac{\partial \rho}{\partial y} h_N^2 - g \rho_0 \frac{\partial \eta}{\partial y} h_N. \quad (2)$$

Here,  $\partial \rho / \partial y$  is the horizontal density gradient,  $\eta$  is the sea surface height and  $h_N$  is the water depth,  $\rho_0 = 1030 \text{ kg m}^{-3}$  is the reference density of seawater,  $g = 9.81 \text{ m s}^{-2}$  is the gravitational acceleration. In (2),  $\partial \rho / \partial y$  is assumed to be constant throughout the water column and does not change with water depth. As the water depth increases, the amount of salt staying in the polynya water column presumably increases, which tends to counterbalance change in the mean polynya water density and maintain the mean density difference between the polynya and ambient waters. Meanwhile,  $\partial \eta / \partial y$  is assumed to be independent of water depth because sea level changes are primarily induced by the wind-driven Ekman pumping in the near surface layer. (2) suggests that  $\tau_{by}$  is negatively related to water depth, which results from the fact that the portion of surface stress being balanced by the barotropic and baroclinic pressure gradient forces increases with water depth. This negative relation is consistent with the sensitivity simulations (G1-Hdepth) of different water depth but the same offshore ocean surface stress showing bottom stress being almost linearly related to  $h_N^{-2}$  (Fig. 10d). Here,  $h_N^{-2}$ , as an inverse function of  $h_N$ , is chosen *empirically* based on the modeled relationship between  $\tau_{by}$  and  $h_N$ . The quasi-linear relationship between  $\tau_{by}$  and  $\tau_{sy}$  at fixed  $h_N$  and the empirical relationship between  $\tau_{by}$  and  $h_N^{-2}$  at fixed  $V_a$  will be used in the scaling analysis in Section 3.

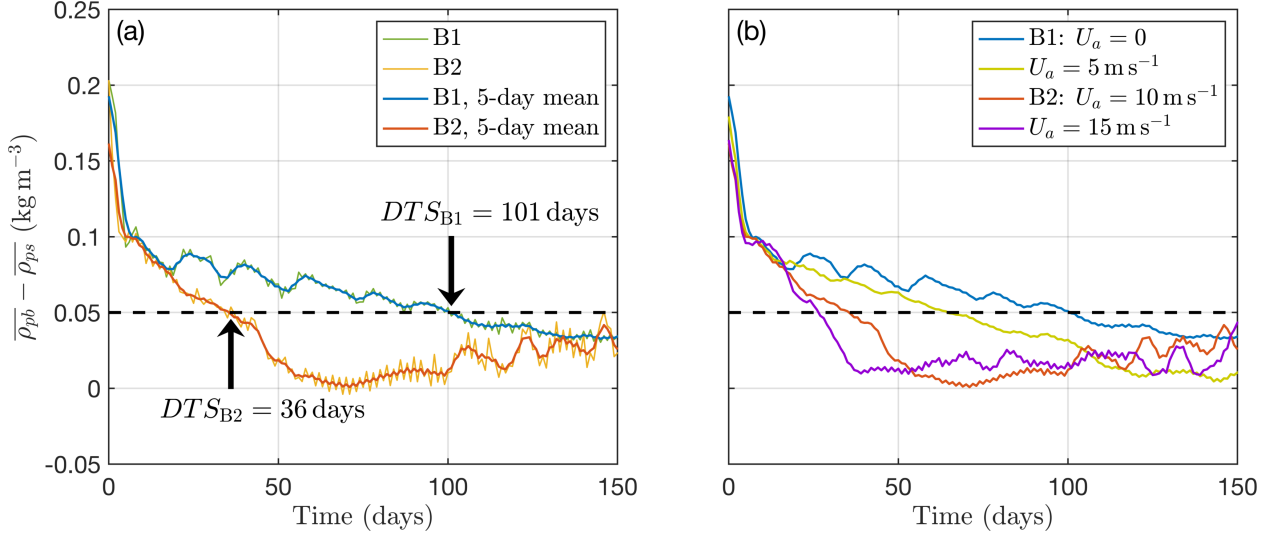
To quantify the influence of different physical factors on the strength of the water column mixing in the polynya region, a metric of the mixing is needed. Here, the time it takes for the water-column stratification in the polynya region to be broken down, which we name destratification timescale (*DTS*), is used. The water-column stratification is considered broken down when the bottom-to-surface density difference ( $\overline{\rho_{pb}} - \overline{\rho_{ps}}$ ) averaged over the polynya area reduces to  $\Delta \rho_{MLD} = 0.05 \text{ kg m}^{-3}$ . Note that this study does not aim to provide the exact time of polynya water column destratification. Rather, *DTS* is used to provide a convenient and objective way to compare the polynya mixing rate in different simulations and to diagnose the influence of various parameters on the mixing. For instance, time series of  $\overline{\rho_{pb}} - \overline{\rho_{ps}}$  in B1 and B2 show dramatically different rates of reduction and, consistently, *DTSs* in B1 and B2 are 36 and 101 days, respectively (Fig. 11a). Comparison of the sensitivity simulations with different alongshore wind speed  $U_a$  shows that reduction rate of  $\overline{\rho_{pb}} - \overline{\rho_{ps}}$  increases with  $U_a$  (Fig. 11b). As a result, *DTS*

418 decreases with increasing  $U_a$ , meaning that polynya vertical mixing is enhanced when strong  
 419 coastal easterly winds are imposed. This is consistent with the onshore Ekman transport driven by  
 420 the easterly winds suppressing offshore transport of the PSW in the upper water column. Influence  
 421 of the other parameters on  $DTS$  will be investigated and compared to results of the scaling analysis  
 422 in Section 4.



423

424 **Fig. 10.** Meridional stresses at the (a) surface ( $\tau_{sy}$ ) and (b) bottom ( $\tau_{by}$ ) of the ocean averaged over Day  
 425 90-100 in Run B1; (c) comparison of  $\tau_{sy}$  and  $\tau_{by}$  averaged in the black boxes in (a) and (b); (d)  $\tau_{by}$  averaged in  
 426 the black boxes in (a) versus  $h_N^{-2}$ , where  $h_N$  is the water depth. The yellow line in (a) outlines the polynya.  
 427



428

429 **Fig. 11.** (a) Daily (thin lines) and 5-day averaged (thick lines) time series of the bottom-to-surface  
 430 density difference ( $\overline{\rho_{pb}} - \overline{\rho_{ps}}$ ) averaged in the polynya region in Runs B1 and B2; (b) 5-day averaged time series  
 431 of  $\overline{\rho_{pb}} - \overline{\rho_{ps}}$  averaged in the polynya region for the cases of different easterly wind speed  $U_a$ . DTS is determined  
 432 in each case as the time of 5-day averaged  $\overline{\rho_{pb}} - \overline{\rho_{ps}}$  first reaching  $0.05 \text{ kg m}^{-3}$ .

433

434 **3. Analytical Scaling**

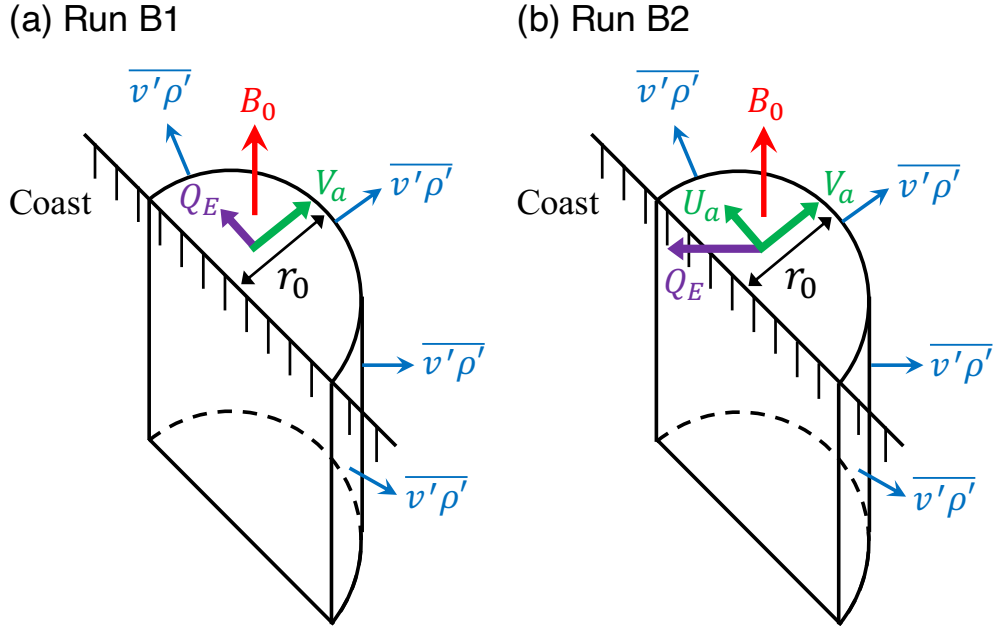
435 An analytical scale of DTS is developed here by considering the major dynamical  
 436 processes in coastal polynyas. The goal is to formulate the influence of various factors (e.g.,  
 437 offshore wind strength, alongshore winds, air temperature, water depth, and initial ambient  
 438 stratification) on water-column mixing in the polynya. Major processes in a polynya with a cross-  
 439 shore width  $r_0$  are illustrated in Fig. 12. The conditions with and without the coastal easterly winds  
 440 are considered. Following Chapman (1999), the change of density within the polynya water  
 441 column is determined by the surface buoyancy flux  $B_0$  from buoyancy loss and the outward  
 442 buoyancy flux on the sides induced by the offshore ocean current. This process can be expressed  
 443 as,

$$\frac{d}{dt} \iiint \rho' dA dz = \iint \frac{\rho_0 B_0}{g} dA - \int \oint \overline{\nu' \rho'} dldz, \quad (3)$$

444 where  $\rho'$  is the density anomaly of the water in the polynya water column relative to the ambient  
 445 water, assuming that the density of the ambient water is fixed.  $A$  is the area of the polynya surface,  
 446  $z$  is the vertical coordinate,  $\nu'$  is the component of the current velocity normal to the polynya

447 boundary,  $l$  is the length of the polynya boundary,  $\overline{v' \rho'}$  is the outward density flux at the edge of  
 448 the polynya averaged both in space and time.

449



450

451 **Fig. 12.** Schematic illustration of the coastal polynya water column in Run (a) B1 and (b) B2 with  
 452 surface buoyancy flux  $B_0$ , lateral density flux  $\overline{v' \rho'}$ , and polynya width  $r_0$ . The green arrows indicate the  
 453 directions of offshore winds  $V_a$  and alongshore winds  $U_a$ . The purple arrows denote the direction of Ekman  
 454 transport  $Q_E$ .

455

456 *a. Scaling of DTS*

457 As the density of the polynya surface water increases, it sinks down and erodes  
 458 stratification in the polynya water column. Considering the one-dimensional downward convective  
 459 penetration of a PSW plume in a linearly stratified water column and assuming no lateral spreading  
 460 of the PSW, Turner (1973) gave a solution of the depth of the growing surface mixed layer  
 461 (Visbeck et al. 1996):

$$462 \quad h = \frac{(2Bt)^{0.5}}{N}. \quad (4)$$

463 Here,  $B$  is the surface buoyancy flux,  $t$  is time, and  $N$  is buoyancy frequency. A scale of the *DTS*,  
 464 i.e., the time of the PSW plume reaching the bottom of the polynya water column with depth  $h_N$ ,  
 465 can thus be obtained from (4) as,

$$DTS = k \frac{h_N^2 N^2}{2B_e}. \quad (5)$$

466 Here,  $k$  is a proportionality constant between  $DTS$  and the time in (4);  $N =$   
 467  $[-(g\Delta\rho_0)/(\rho_0 h_N)]^{1/2}$  varies with the initial surface-to-bottom density difference  $\Delta\rho_0$  in the  
 468 polynya;  $B_e$  is the *effective surface buoyancy flux*, which counts only the part of the total buoyancy  
 469 flux,  $B_0$ , remaining in the polynya water column and excludes the rest that has been laterally  
 470 carried away from the polynya region. Considering the wind-driven circulation in Section 2b,  $B_e$   
 471 can be expressed as,

$$B_e = B_0 - (B_t - B_c) = (1 - c)B_0. \quad (6)$$

472  
 473 Here,  $B_t$  is the part of the surface buoyancy flux being transported away from the polynya by the  
 474 wind-driven offshore current, and is positive for outward transport across the polynya boundary;  
 475  $B_c$  is the correction term to  $B_t$ , representing the reduction of offshore transport due to any onshore  
 476 flow, such as the Ekman transport driven by the coastal easterly winds;  $c$  is the ratio of total  
 477 offshore transport ( $B_t - B_c$ ) to the surface buoyancy flux  $B_0$ . Note that the original expressions in  
 478 Turner (1973) are restored when  $k = 1$  and  $B_t = B_c = 0$ .

479  
 480 *b. Scaling of  $B_0$*

481 When the alongshore winds are absent or weak, the total wind speed can be approximated  
 482 by the offshore wind speed. Based on the thermodynamic model of a coastal polynya in Pease  
 483 (1987) and Chapman (1999), considering sensible and latent heat fluxes at the surface,  $B_0$  can be  
 484 expressed as,

$$B_0 = \frac{C_t g \Delta\rho_s \rho_a V_a}{L_f \rho_0 \rho_i} [C_p (T_0 - T_a) + L_e (q_0 - q_a)], \quad (7)$$

485 where  $C_t = 2 \times 10^{-3}$  is the transfer coefficient at 2 m height for sensible and latent heat fluxes;  
 486  $\Delta\rho_s$  is the density change due to brine rejection;  $\rho_a = 1.3 \text{ kg m}^{-3}$  is the air density;  $L_f =$   
 487  $3.34 \times 10^5 \text{ J kg}^{-1}$  is the latent heat of fusion of water;  $\rho_i = 910 \text{ kg m}^{-3}$  is the density of sea ice;  
 488  $C_p = 1004 \text{ J}^\circ \text{C}^{-1} \text{ kg}^{-1}$  is the specific heat of air;  $T_a$  and  $T_0$  are the temperature of air at 2 m

489 height and temperature of water at the surface of the ocean, respectively;  $L_e = 2.5 \times 10^6 \text{ J kg}^{-1}$   
 490 is the latent heat of water evaporation;  $q_a$  is the specific humidity at 2 m height; and  $q_0$  is the  
 491 saturation specific humidity at  $T_0$ . Following the wintertime observations in the TNBP (Guest  
 492 2021a), we assume  $q_a = 5 \times 10^{-4}$  in the scaling analysis and numerical model. Since the polynya  
 493 surface water is nearly frozen,  $T_0 = -1.8 \text{ }^\circ\text{C}$ , which corresponds to  $q_0 = 3.3 \times 10^{-3}$ . Assuming  
 494 the fraction of the salt being rejected during sea ice formation is 70% (Chapman 1999),  $\Delta\rho_s$  is  
 495  $21 \text{ kg m}^{-3}$ . Note that in the analytical derivations,  $V_a$  is used to represent the total wind speed in  
 496 the calculations of buoyancy loss and surface stresses for simplicity. Tests with the full expression  
 497 of total wind speed,  $(V_a^2 + U_a^2)^{0.5}$ , give negligible changes of the computed *DTS* (not shown).

498

499 *c. Scaling of  $B_t$*

500 Using Equation (3), the offshore transport of buoyancy flux  $B_t$  at an equilibrium state can  
 501 be estimated by vertically integrating the outward density flux  $\overline{v'\rho'}$  across the polynya edge,

$$\iint \frac{\rho_0 B_t}{g} dA = \int \oint_{out} \overline{v'\rho'} dldz. \quad (8)$$

502 Here,  $\overline{v'\rho'}$  can be scaled as,

$$\overline{v'\rho'} \sim V_0 \Delta\rho, \quad (9)$$

503 where  $V_0$  is the mean ocean current speed, and  $\Delta\rho$  is the density anomaly of the polynya water  
 504 relative to the ambient water. Note that, even though the form of  $\overline{v'\rho'}$  in (9) is the same as that in  
 505 Chapman (1999), the transport process that (9) represents differs from that in Chapman (1999).  
 506 Chapman (1999) considered only the lateral buoyancy dispersal caused by the near-bottom eddies  
 507 generated by baroclinic instability of the thermal-wind-balanced density front on the polynya rim.  
 508 Our analysis shows that much of the lateral buoyancy dispersal in Antarctic polynyas occurs in the  
 509 upper part of the water column resulting from the offshore mean flow induced by the offshore  
 510 katabatic winds. It is likely that, near the bottom, both wind-driven flows and baroclinic eddies  
 511 can induce circulation and disperse the PSW. For simplicity, the scaling analysis in this study  
 512 considers only the buoyancy dispersal induced by the wind-driven circulation. The density  
 513 anomaly  $\Delta\rho$  is assumed to be proportional to  $\Delta\rho_s$ , which is the density increase due to brine

514 rejection.  $V_0$  is evaluated using the aforementioned quasi-linear relationship between the  
 515 meridional *bottom* stress  $\tau_{by} = -\rho_0 C_{D0} V_0^2$  and the meridional *surface* stress  $\tau_{sy} = \rho_a C_{Da} V_a^2$ , and  
 516 the quasi-linear relationship between  $\tau_{by}$  and  $h_N^{-2}$ . Here,  $C_{D0} = 2.5 \times 10^{-3}$  is the quadratic  
 517 bottom drag coefficient (Lentz 2008),  $\tau_{sy}$  is dominated by the offshore meridional wind stress,  
 518  $C_{Da}$  is the air-ocean drag coefficient and, as in the numerical model, follows the expression from  
 519 Large and Yeager (2004),

$$C_{Da} = \left( \frac{2.7}{V_a} + 0.142 + 0.0764 V_a \right) \times 10^{-3}. \quad (10)$$

520 Using the quasi-linear relationships between  $\tau_{by}$  and  $\tau_{sy}$  and between  $\tau_{by}$  and  $h_N^{-2}$ , we obtain an  
 521 expression of  $V_0$  as

$$V_0 \sim \frac{\alpha}{h_N} \left( \frac{C_{Da} \rho_a}{C_{D0} \rho_0} \right)^{0.5} V_a. \quad (11)$$

522 Here,  $\alpha$  is a constant vertical length scale introduced to maintain dimensional consistency, and its  
 523 value will be determined empirically from the sensitivity simulations (Section 4).

524 For a polynya with initially constant buoyancy frequency  $N$ , area  $A$ , and perimeter  $M$ ,  
 525 using Equation (8)-(11), Equation (8) can be expanded as,

$$\frac{\rho_0 B_t A}{g} = \alpha \left( \frac{C_{Da} \rho_a}{C_{D0} \rho_0} \right)^{0.5} V_a \Delta \rho_s M. \quad (12)$$

526 Rearranging Equation (12), the offshore buoyancy flux  $B_t$  can be expressed as,

$$B_t = \frac{\alpha V_a \Delta \rho_s g}{\rho_0 (A/M)} \left( \frac{C_{Da} \rho_a}{C_{D0} \rho_0} \right)^{0.5}. \quad (13)$$

527

528 *d. Scaling of  $B_c$*

529 We now seek to derive a scaling formula for the onshore Ekman transport driven by the  
 530 coastal easterly winds. Its influence is measured by  $B_c$ , a correction to  $B_t$ , as described in Equation  
 531 (6). Similar to Equation (8),  $B_c$  can be obtained by vertically integrating the inward density flux  
 532 across the polynya edge,

$$\frac{\rho_0 B_c}{g} A = \epsilon P \Delta \rho \int v_E dz, \quad (14)$$

533 where  $\epsilon$  is the efficiency of the onshore lateral buoyancy flux transport induced by Ekman  
 534 dynamics and accounts for the influences of factors, such as irregular polynya shape or vertically  
 535 varying density anomaly, that cannot be considered explicitly in a first-order scaling analysis,  $v_E$   
 536 is the horizontal Ekman velocity. Under the coastal easterly winds of speed  $U_a$ , the net Ekman  
 537 transport is  $\int v_E dz = \tau_E / (\rho_0 |f|)$ , where  $\tau_E = \rho_a C_{Da} V_a U_a$  is the westward alongshore wind stress,  
 538  $f$  is the Coriolis frequency. Equation (14) then gives,

$$B_c = \frac{\epsilon \Delta \rho_s g \rho_a C_{Da} V_a U_a}{\rho_0^2 |f| (A/M)}. \quad (15)$$

539 Since  $B_c$  is a reduction term to  $B_t$ , it has to satisfy  $B_c \leq B_t$ , which set a lower bound of  $DTS$  at the  
 540 extreme scenario of the onshore Ekman transport of the PSW completely balancing the offshore  
 541 transport.

542

543 *e. Scaling of Polynya Cross-shore Width  $r_0$*

544 The factor,  $A/M$ , in Equations (13) and (15), the ratio of the polynya area and perimeter,  
 545 is presumably proportional to the cross-shore width of the polynya,  $r_0$ . Following Pease (1987),  
 546 under constant wind forcing,  $r_0$  can be estimated from the balance between the wind-driven  
 547 offshore advection of the sea ice (which tends to widen the polynya) and the resistance due to  
 548 growth of the offshore sea ice. The expression of the maximum polynya cross-shore width can be  
 549 written as (Chapman 1999),

$$550 \quad r_{0max} = \frac{\kappa V_i}{B_0}, \quad (16)$$

551 where  $\kappa = \Delta \rho_s g h_i / \rho_0$ ,  $h_i$  is the collection thickness of frazil ice, and  $V_i$  is the offshore sea ice  
 552 speed at the edge of the polynya, which is approximated as 3% of the offshore wind speed  
 553 (Martinson and Wamser 1990). That is,  $V_i \approx 0.003 V_a$ . Many studies have considered the  
 554 parameterizations of  $h_i$  (e.g., Bauer and Martin 1983; Biggs et al. 2000; Winsor and Björk 2000)  
 555 and given an average value of  $\sim 0.2$  m under oscillating winds. This value is also consistent with

556 observed thickness of consolidated ice at the edge of the TNBP (Tison et al. 2020). For simplicity,  
 557  $h_i$  is set to 0.2 m here.

558 For oscillating winds, if the wind period is much shorter than the ocean response timescale,  
 559 the timescale of water column mixing can be assumed to be independent of the wind period  
 560 (Chapman 1999), and the polynyas are persistently open with the width of  $r_{0max}$ . Hence, the  
 561 dependency of  $r_0$  on the wind oscillation period  $P_{wind}$  is neglected in the scaling analysis here  
 562 even though offshore winds fluctuate in reality and our numerical models. Therefore,  $A/M$  can be  
 563 scaled based on (16) as,

$$\frac{A}{M} \propto r_0 = \frac{0.03\kappa V_a}{B_0} = \frac{0.03\Delta\rho_s g h_i V_a}{\rho_0 B_0}. \quad (17)$$

564 Note that neglecting the influence of  $P_{wind}$  here results in the final scaling of *DTS* being  
 565 independent of  $P_{wind}$ . This will be validated in Section 4.

566 With (7) and (17),  $A/M$  and  $r_0$  become independent of the offshore mean wind speed  $V_a$ .  
 567 This is valid when  $V_a$  is high and air temperature  $T_a$  is low (Van Woert 1999). According to our  
 568 numerical simulations, the offshore winds can effectively keep the polynya open when the offshore  
 569 winds are in the katabatic regime with the maximum wind speed  $2V_a \geq 25 \text{ m s}^{-1}$ . Applying  
 570 Equation (17) with the atmospheric condition used in Run B1 gives  $r_0 \approx 28 \text{ km}$ , which is  
 571 consistent with the cross-shore width of the modeled polynya (Fig. 5a).

572 Combining Equations (7), (13), (15) and (17), we obtain the coefficient  $c$  in Equation (6)  
 573 as,

$$c = \frac{100}{3h_i} \left[ \alpha \left( \frac{C_{Da}\rho_a}{C_{D0}\rho_0} \right)^{0.5} - \frac{\epsilon C_{Da}\rho_a U_a}{\rho_0 |f|} \right]. \quad (18)$$

574 Equations (5), (6), (7), and (18) together provide a complete scaling formula for *DTS*:

$$575 DTS = \frac{k \frac{\rho_0 \rho_i}{\Delta \rho_s \rho_a} L_f h_N^2 N^2}{2 C_t g V_a \left\{ 1 - \frac{100}{3h_i} \left[ \alpha \left( \frac{C_{Da}\rho_a}{C_{D0}\rho_0} \right)^{0.5} - \frac{\epsilon C_{Da}\rho_a U_a}{\rho_0 |f|} \right] \right\} [C_p(T_0 - T_a) + L_e(q_0 - q_a)]}. \quad (19)$$

576 Note that most of the variables in (19) are known quantities and the air-sea drag coefficient,  $C_{Da}$ ,  
 577 is provided in (10). The independent variables, i.e., the sensitivity parameters considered in this

578 study, are  $V_a$ ,  $U_a$ ,  $T_a$ ,  $N$ , and  $h_N$ . There are three constant coefficients: i) the proportionality  
 579 constant between  $DTS$  and time in Turner's MLD formula,  $k$ , ii) the vertical length scale  
 580 incorporating the efficiency of the wind-driven offshore transport carrying PSW offshore,  $\alpha$ , and  
 581 iii) the efficiency of the onshore lateral buoyancy flux transport induced by Ekman dynamics,  $\epsilon$ .

582 Even with the simplifications we have employed in the scaling analysis, Equation (19)  
 583 remains complex and difficult to use for comparing the times required to break down the  
 584 stratification in polynyas. Here, we seek to distill it to provide an intuitive understanding of the  
 585 key mechanism. Recognizing (19) and combining it with (18), we obtain,

$$DTS = \frac{h_N}{(1-c)[gV_a/(h_N N^2)]} \frac{k \frac{\rho_0 \rho_i}{\Delta \rho_s \rho_a} L_f}{2C_t[C_p(T_0 - T_a) + L_e(q_0 - q_a)]}. \quad (20)$$

586 Considering the offshore wind speed  $V_a$  as the key forcing to produce the surface buoyancy flux  
 587 that gradually erodes the stratification in the polynya water column, and neglecting the constants  
 588 and other factors with relatively weak influence in (20), the  $DTS$  scaling can be simplified as,

$$DTS \sim \frac{h_N}{(1-c)E}. \quad (21)$$

589 Here,  $E = gV_a/(h_N N^2)$  is the stratification erosion rate, which increases with increasing  $V_a$  and  
 590 decreasing  $h_N$  and  $N$ . It is affected by the offshore loss and onshore compensation of the lateral  
 591 buoyancy flux, which are included in the coefficient  $c$ , as shown by (18). Equation (21) is  
 592 presumable applicable to gain a qualitative understanding of the key destratification processes in  
 593 Antarctic coastal polynya. Overall, the scaling analysis here provides a framework for i)  
 594 investigating the influence of different factors on water column mixing in Antarctic coastal  
 595 polynyas, ii) analyzing the variability of DSW formation across different Antarctic polynyas, and  
 596 iii) understanding the temporal (e.g., interannual or longer-term) variability of stratification in a  
 597 polynya, including a qualitative prediction of the future polynya mixing. For these purposes, values  
 598 of the coefficients,  $k$ ,  $\alpha$ , and  $\epsilon$ , need to be determined, and the depicted dynamical relationships  
 599 between the physical parameters and  $DTS$  need to be validated. These are the goals of the next  
 600 section.

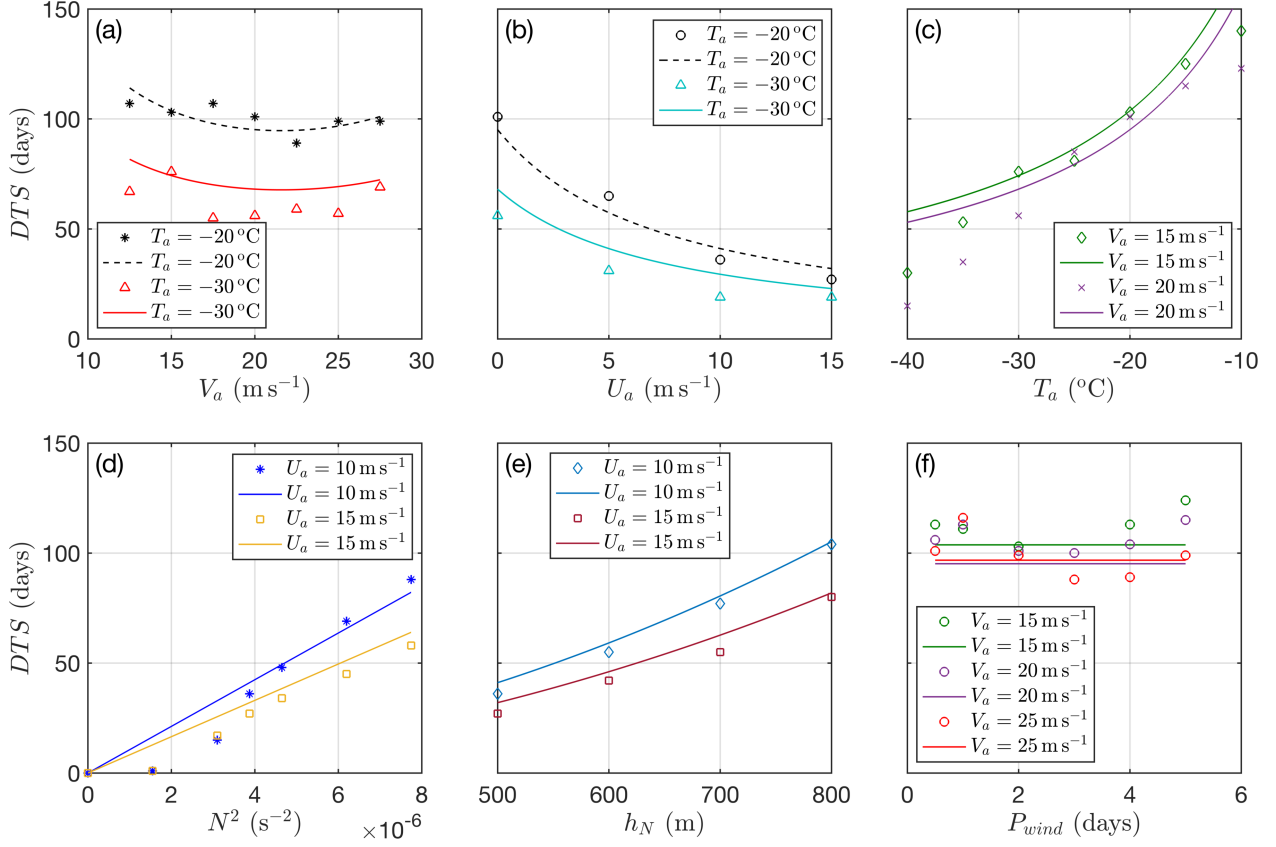
601  
 602

603 **4. Sensitivity Simulations**

604 Here, values of  $k$ ,  $\alpha$ , and  $\epsilon$ , in (19) are to be determined first through fitting scaled  $DTS$   
605 values to corresponding values given by simulations in the *calibration* sensitivity sets: G1-Vwind  
606 with variable  $V_a$  and G1-Uwind with variable  $U_a$ . Applying parameter values used in each of the  
607 10 calibration simulations to (19) gives an expression of scaled  $DTS$  with  $k$ ,  $\alpha$ , and  $\epsilon$  as dependent  
608 coefficients. Least-squares fitting of the scaled  $DTS$  to the corresponding values extracted from  
609 the 7 simulations in G1-Vwind gives  $k = 4.49$ ,  $\alpha = 0.138$  m, and a qualitative match between the  
610 scaled and modeled  $DTS$  (black symbols and the black dashed line in Fig. 13a); and least-squares  
611 fitting to the  $DTS$  values extracted from the 4 simulations in G1-Uwind gives  $\epsilon = 0.015$  and also  
612 a qualitative match between the scaled and modeled  $DTS$  (black symbols and the black dashed line  
613 in Fig. 13b). Because of the fittings, all 10 calibration cases together show a great match between  
614 analytically scaled and modeled  $DTS$  with a R-squared value of 0.96 (Fig. 14a). The validation of  
615 the scaling will be carried out below with the validation simulations.

616 With the fitted coefficients, the scaled  $DTS$  shows a weak quadratic-like dependence on  
617 the offshore wind speed,  $V_a$ , qualitatively matching that given by simulations in G1-Vwind (Fig.  
618 13a). The weak quadratic-like relationship results from the dependence of both the surface  
619 buoyancy flux,  $B_0$  and the air-sea drag coefficient,  $C_{Da}$ , on  $V_a$ , as shown in (7) and (10),  
620 respectively. In particular, under mild winds, the analytically derived  $DTS$  decreases with  
621 increasing  $V_a$ , reflecting the dominant positive influence of offshore winds on  $B_0$  and the intensity  
622 of polynya water column mixing. When the offshore winds become much stronger,  $C_{Da}$  increases  
623 much faster, and the increase of  $B_t$  outperforms  $B_0$ . This reduces the amount of PSW remaining  
624 in the polynya region, and  $DTS$  thus increases with  $V_a$ . Therefore, within the katabatic regime  
625 considered here, the dependence of  $DTS$  on  $V_a$  is weak because of the competition between  $B_0$  and  
626  $B_t$ . We stress here that these differ from results of previous studies that neglect the wind-driven  
627 offshore loss of the PSW in the upper water column and consider only the direct influence of  $V_a$   
628 on  $B_0$ . In those studies,  $DTS$  should monotonically decrease with increasing  $V_a$ .

629



631 **Fig. 13.** Comparisons of numerically modeled  $DTS$  (symbols) and analytically derived  $DTS$  (lines) in  
632 sensitivity sets with varying values of (a) mean offshore wind speed, (b) alongshore wind speed, (c) air  
633 temperature, (d) initial ambient stratification, (e) water depth, and (f) oscillation period of the offshore winds.  
634 The black symbols in (a) and (b) are from simulations in the calibration sets (G1-Vwind and G1-Uwind) used to  
635 obtain the coefficients in the analytically scaled formulae through least squares fitting, and the black dashed lines  
636 in (a) and (b) are results of the fittings. Other symbols in (a-b) and all symbols in (c-f) are from validation sets;  
637 all solid lines are obtained from Equation (18) with fitted coefficients and thus independent of the corresponding  
638 simulations.

639 Meanwhile, the scaled  $DTS$  shows a negative dependence on the alongshore wind speed,  
640  $U_a$  (Fig. 13b). This is consistent with stronger coastal easterly winds driving stronger onshore  
641 Ekman transport, keeping more PSW in the polynya region, and causing faster mixing of the  
642 polynya water column. This result emphasizes that wind direction can significantly change vertical  
643 mixing in Antarctic coastal polynyas. Note that to ensure  $B_c \leq B_t$ ,  $U_a$  is chosen to be no more than  
644  $15 \text{ m s}^{-1}$  in both numerical and scaling analyses. This aligns with previous research showing the  
645 mean alongshore wind speed being around  $10 \text{ m s}^{-1}$  in winter over most Antarctic coastal polynyas  
646 (Nihashi and Ohshima 2015).

647 To validate the scaled formula, we compare scaled and modeled  $DTS$  in the 11 validation  
648 sets, including G2-Vwind and G2-Uwind, which are similar to G1-Vwind and G1-Uwind,

649 respectively, but with air temperature,  $T_a$ , changed from the control value of -20°C to -30°C (Table  
650 2). Comparisons in all validation sets show qualitatively similar dependence of scaled and modeled  
651  $DTS$  on the 6 sensitivity parameters (Fig. 13). In particular, both modeled and scaled  $DTS$  show  
652 positive dependence on  $T_a$  (Fig. 13c), reflecting the fact that, as air temperature increases,  $B_0$  in  
653 Equation (7) decreases with weakened buoyancy loss, and  $DTS$  increases. However, the  
654 relationship is nonlinear, and mismatch between the scaled and modeled results remains. This is  
655 likely caused by other influencing pathways, such as air temperature affecting sea ice strength,  
656 polynya size, and then polynya mixing, being captured by the numerical model, but not considered  
657 in the analytical scaling.

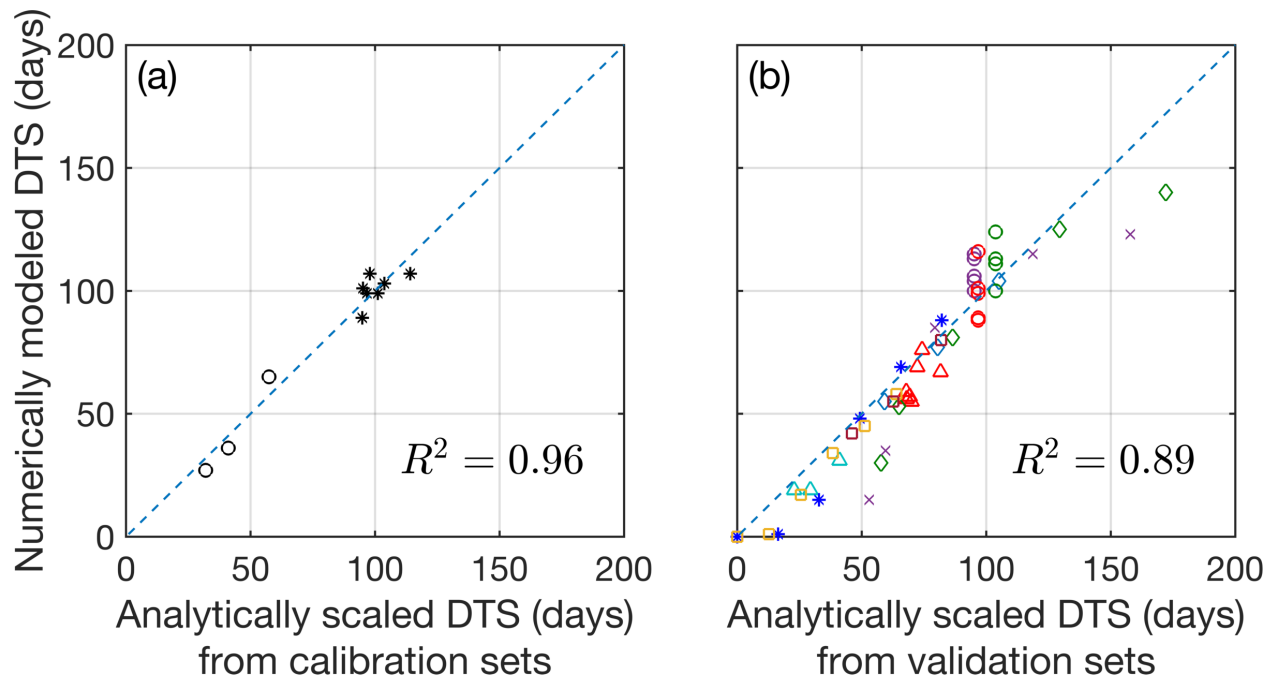
658 Both the modeled and scaled  $DTS$  show positive dependence on the initial ambient  
659 stratification,  $N^2$  (Fig. 13d). This reflects the tendency of existing vertical stratification  
660 suppressing downward penetration of the PSW. For instance, with small  $N^2$ , PSW sinks quickly  
661 to the bottom, resulting a small  $DTS$ . Therefore, the pre-conditioning of the stratification in a  
662 polynya before the winter months should be taken into account when we study polynya water  
663 column mixing. The small mismatch between the modeled and scaled dependence of  $DTS$  on  $N^2$   
664 at low  $N^2$  likely results from the bottom-to-surface density difference threshold used in the  
665 modeling analysis. Because the water column is considered well-mixed when the bottom-to-  
666 surface density difference in the model is smaller than  $0.05 \text{ kg m}^{-3}$ ,  $DTS$  should be 0 when  $N^2$  is  
667 lower than  $10^{-6} \text{ s}^2$ , which is consistent with the trend of modeled  $DTS$  (Fig. 13d). Using a smaller  
668 density difference in the  $DTS$  definition would reduce the model-scaling mismatch at low  $N^2$ , but  
669 it would significantly increase the simulation time required for the water column to reach  
670 destratification. Because the threshold value does not affect the dynamical interpretation,  $0.05 \text{ kg}$   
671  $\text{m}^{-3}$  is kept here for a convenient comparison among the simulations. Meanwhile, as the water  
672 depth,  $h_N$ , increases, both the modeled and scaled  $DTS$  increase since more time is required for  
673 the PSW to reach a deeper bottom (Fig. 13e).

674 Because the wind oscillation period,  $P_{wind}$ , is not considered in the analytical scaling, the  
675 scaled  $DTS$  does not vary with  $P_{wind}$  (Fig. 13f). Simulations in G1-Pwind, G2-Pwind and G2-  
676 Pwindx all show weak dependence of  $DTS$  on  $P_{wind}$  with no clear trend. This is consistent with  
677  $P_{wind}$  considered here (2-5 days) being smaller than the ocean response timescale of >10 days, as  
678 well as wind-induced high-frequency oscillations of  $\overline{\rho_{pb}} - \overline{\rho_{ps}}$  being relatively small (Fig. 11a). It

679 is likely that wind oscillation of longer periods will have a more pronounced influence on the  
 680 polynya water-column mixing, which is not addressed here.

681 We have also considered the influence of Coriolis parameter,  $f$ , by moving the model  
 682 domain southward by  $10^\circ$  latitude, which covers the latitude range of most Antarctic coastal  
 683 polynyas. These simulations (not shown) give very similar results as B1 and B2. This is not  
 684 surprising because  $f$  changes only 6% with the  $10^\circ$  latitude shift. Because both  $f$  and  $U_a$  affect  
 685  $DTS$  through the onshore Ekman transport and they appear together in (19), the influence of  $f$  can  
 686 directly be compared to that of  $U_a$ . Simulations in G1-Uwind and G2-Uwind show that changing  
 687  $U_a$  by 6%, i.e.,  $0.6 \text{ m s}^{-1}$ , has negligible impact on  $DTS$  (Fig. 13b).

688



689  
 690  
 691  
 692

**Fig. 14.** Comparisons of numerically modeled and analytically scaled  $DTS$  from (a) calibration sets and  
 (b) validation sets. The shapes of the symbols are consistent with those in Fig. 13.

693 Combining all 11 validation sets together, the scaled *DTS* show a general alignment with  
694 the model results with a R-squared value of 0.89 (Fig. 14b). This alignment with the output of the  
695 independent validation simulations confirms that the scaling analysis captures the major dynamical  
696 processes of the modeled polynyas and demonstrates that the scaled formula can be used to  
697 qualitatively examine the influence of the considered parameters on the polynya mixing.

698

## 699 **5. Discussion**

700 Considering the influence of winds, sea ice and ice shelf, this study demonstrates that water  
701 column mixing and PSW formation in Antarctic coastal polynyas, as well as intrusion of the PSW  
702 into the neighboring ice shelf cavity are directly impacted by three-dimensional ocean circulation  
703 in the polynya region. Offshore transport of the PSW in the upper part of the water column induced  
704 by the katabatic offshore winds can be a major loss of the PSW in the polynya and substantially  
705 reduce the strength of the local vertical mixing. Meanwhile, through generating onshore Ekman  
706 transport, the prominent coastal easterly winds along the Antarctic coast could suppress lateral loss  
707 of the buoyancy flux toward the offshore and enhance vertical mixing in the polynya region. Note  
708 that because the conditions considered here are highly simplified, the absolute values of the *DTS*  
709 obtained here cannot be directly applied to any particular Antarctic coastal polynya. Moreover,  
710 while the scalings of the surface buoyancy loss and the onshore Ekman transport are based on  
711 fundamental physics, the derivation of the offshore transport relies on an empirical relationship  
712 between the surface stress and water depth, which may not necessarily be applicable to all  
713 situations. However, as the parameter space considered here is representative of many Antarctic  
714 coastal polynyas, the captured dynamics and parameter dependences are robust. For instance,  
715 observations in both the Cape Darnley Polynya (Ohshima et al. 2013) and Mertz Polynya (Martin  
716 et al. 2017; Snow et al. 2016) show flow directions of the DSW being aligned with the  
717 northwestward offshore winds, which is consistent with our model result.

718 This work emphasizes the impact of wind-driven ocean current on the PSW transport and  
719 destratification process. It stresses the importance of considering the influence of winds and sea  
720 ice when studying polynya dynamics. This is missing in previous studies of polynya dynamics  
721 (e.g., Årthun et al. 2013; Chapman and Gawarkiewicz 1997; Chapman 1998; 1999; Visbeck et al.

722 1996; Wilchinsky and Feltham 2008; Zhang and Cenedese 2014) where the sea ice dynamics and  
723 air-sea momentum transfer are neglected.

724 Circulations in real Antarctic coastal polynyas are complex and also affected by other  
725 factors, such as variable offshore and upstream conditions, irregular seafloor bathymetry (e.g.,  
726 troughs, depressions and banks), frazil ice, ice tongues, icebergs, and complex coastlines, which  
727 are not considered in this study. For instance, studies have demonstrated that troughs on the  
728 Antarctic shelf can facilitate intrusion of the Circumpolar Deep Water toward the Antarctic coast  
729 (e.g., St-Laurent et al. 2013), and depressions on the shelf could accumulate the PSW (e.g.,  
730 Williams et al. 2008). Frazil ice formation has been shown as an important component in the DSW  
731 formation in polynyas (Ohshima et al. 2022). All of these could potentially modify the  
732 stratification in the coastal polynyas. Moreover, ambient shelf and slope circulation could also  
733 affect the polynya flows and PSW dispersal pattern. For instance, because polynyas on the Eastern  
734 Antarctic coast are adjacent to the shelf break (Tamura et al. 2016), the Antarctic Slope Current  
735 (Stewart et al. 2019) may affect the zonal transport of the PSW. Therefore, to understand the water  
736 column mixing in a specific polynya would require investigation of the influence of all these  
737 factors as well. Moving toward that direction and also motivated by the condition at the TNBP,  
738 Part II of this study will examine how a neighboring ice tongue and a nearby headland can modify  
739 polynya circulation and mixing.

740

## 741 **6. Summary**

742 This study examines the dynamics of various physical factors influencing wintertime PSW  
743 formation and water column mixing in Antarctic coastal polynyas. This Part I work combines  
744 process-oriented idealized simulations and dynamical scaling analysis, to investigate the influence  
745 of offshore winds, alongshore winds, air temperature, initial stratification, and water depth on the  
746 polynya destratification timescales. The time required to destratify the polynya water column, the  
747 destratification timescale (*DTS*), is chosen to represent the strength of polynya water column  
748 mixing as it is directly related to the potential of DSW production in a polynya within a winter.  
749 The idealized polynya configurations considered here represent typical conditions of some  
750 Antarctic coastal polynyas. The numerical simulations qualitatively capture fundamental  
751 hydrographic and sea ice processes in polynya regions depicted by satellite images and in situ

752 observations. The model simulations show that much of the PSW is directly transported offshore  
753 by the wind-driven offshore flow and does not contribute to vertical mixing in the polynya water  
754 column (Figs. 5–6). Meanwhile, onshore Ekman transport induced by the alongshore easterly  
755 winds, a common feature of many Antarctic coastal regions, can suppress the offshore loss of the  
756 PSW and enhance vertical mixing in coastal polynyas (Figs. 6–7). These suggest that the polynya  
757 water column mixing is directly affected by three-dimensional circulation in the polynya region  
758 and that including the effects of both katabatic and alongshore winds is necessary for capturing  
759 characteristics of the polynya mixing.

760 To synthesize the influence of the physical factors, analytical scaling of polynya  
761 destratification timescales is performed (Section 3). The derived formula, Equation (19), is  
762 validated against numerical sensitivity simulations (Section 4). General agreement between the  
763 scaled and modeled *DTS* confirms that the scaling analysis capture fundamental dynamics of the  
764 coastal polynyas (Figs. 13–14), including dependence of the destratification timescale on a number  
765 of physical factors: i) Stronger offshore katabatic winds can both *enhance* the polynya mixing  
766 through generating more PSW and *suppress* the mixing through transport more PSW offshore at  
767 the same time, which results in a nonlinear relationship between *DTS* and the offshore wind speed;  
768 ii) Typical period of offshore wind oscillation has little impact on the polynya mixing because it  
769 is shorter than the ocean response timescale; iii) Stronger coastal easterly winds drive stronger  
770 onshore Ekman transport, cause weaker offshore loss of the PSW, and result in faster  
771 destratification of the polynya water column; iv) Higher air temperature reduces the sea ice and  
772 PSW formation, and then weakens polynya mixing; and v) stronger initial stratification of the  
773 water column suppresses mixing and slows down polynya destratification.

774 The process-oriented simulations, the derived scaling formula, and the dynamical  
775 relationships presented in this study provide a framework to investigate the influence of other  
776 physical factors on water column mixing in Antarctic coastal polynyas, to compare the DSW  
777 formation in different polynyas, and to understand temporal evolution of PSW formation in a  
778 polynya for given large-scale environmental changes. Moving toward that direction, Part II of this  
779 study will investigate the influence of an ice tongue and headland on the polynya mixing. Future  
780 studies should analyze the influence of other factors, such as bathymetry and upstream conditions.  
781 These studies together would provide a path toward parameterization of polynya processes in  
782 large-scale, low-resolution models that cannot explicitly resolve small-scale polynya processes.

783 *Acknowledgments.*

784 This study is supported by the National Science Foundation through grants OPP-1643735,  
785 OPP-1643901, and OPP-2021245. YX and WGZ are also supported by OPP-2205008.

786

787 *Data Availability Statement.*

788 The MODIS image was obtained from the Worldview tool from NASA's Earth Observing  
789 System Data and Information System at <https://worldview.earthdata.nasa.gov/>. The Sentinel-1  
790 image processed by ESA was downloaded from NASA's Distributed Active Archive Centers  
791 operated by the Alaska Satellite Facility at <https://ASF.alaska.edu/>. The marine mammal data were  
792 collected and made freely available at <http://www.meop.net> by the International MEOP  
793 Consortium and the national programs that contribute to it. The meteorological station data were  
794 obtained from the Australian Antarctic Data Center at  
795 [https://data.aad.gov.au/metadata/records/Antarctic\\_Meteorology](https://data.aad.gov.au/metadata/records/Antarctic_Meteorology). The model code and scripts  
796 used to conduct the simulations and analyses in this study are available at  
797 <https://doi.org/10.5281/zenodo.7735630>.

798

799 REFERENCES

800 Adolphs, U., and G. Wendler, 1995: A pilot study on the interactions between katabatic winds and  
801 polynyas at the adélie coast, eastern Antarctica. *Antarct. Sci.*, **7**, 307–314,  
802 <https://doi.org/10.1017/S0954102095000423>.

803 Aoki, S., K. Ono, D. Hirano, and T. Tamura, 2020: Continuous winter oceanic profiling in the  
804 Cape Darnley Polynya, East Antarctica. *J. Oceanogr.*, **76**, 365–372,  
805 <https://doi.org/10.1007/s10872-020-00550-w>.

806 Arrigo, K. R., and G. L. van Dijken, 2003: Phytoplankton dynamics within 37 Antarctic coastal  
807 polynya systems. *J. Geophys. Res. Ocean.*, **108**, <https://doi.org/10.1029/2002jc001739>.

808 Årthun, M., P. R. Holland, K. W. Nicholls, and D. L. Feltham, 2013: Eddy-Driven Exchange  
809 between the Open Ocean and a Sub-Ice Shelf Cavity. *J. Phys. Oceanogr.*, **43**, 2372–2387,  
810 <https://doi.org/10.1175/JPO-D-13-0137.1>.

811 Barnes-Keoghan, I., 2000: Antarctic Climate Data Collected by Australian Agencies, Ver. 1,  
812 Australian Antarctic Data Centre, accessed 2 May 2021,  
813 [https://data.aad.gov.au/metadata/records/Antarctic\\_Meteorology](https://data.aad.gov.au/metadata/records/Antarctic_Meteorology).

814 Bauer, J., and S. Martin, 1983: A model of grease ice growth in small leads. *J. Geophys. Res.*, **88**,  
815 2917–2925, <https://doi.org/10.1029/JC088iC05p02917>.

816 BIGGS, N. R. T., M. A. MORALES MAQUEDA, and A. J. WILLMOTT, 2000: Polynya flux  
817 model solutions incorporating a parameterization for the collection thickness of consolidated  
818 new ice. *J. Fluid Mech.*, **408**, 179–204, <https://doi.org/10.1017/S0022112099007673>.

819 Chapman, D. C., 1998: Setting the Scales of the Ocean Response to Isolated Convection. *J. Phys.*  
820 *Oceanogr.*, **28**, 606–620, [https://doi.org/10.1175/1520-0485\(1998\)028<0606:STSOTO>2.0.CO;2](https://doi.org/10.1175/1520-0485(1998)028<0606:STSOTO>2.0.CO;2).

822 Chapman, D. C., 1999: Dense Water Formation beneath a Time-Dependent Coastal Polynya. *J.*  
823 *Phys. Oceanogr.*, **29**, 807–820, [https://doi.org/10.1175/1520-0485\(1999\)029<0807:DWFBAT>2.0.CO;2](https://doi.org/10.1175/1520-0485(1999)029<0807:DWFBAT>2.0.CO;2).

825 Chapman, D. C., and G. Gawarkiewicz, 1997: Shallow Convection and Buoyancy Equilibration  
826 in an Idealized Coastal Polynya. *J. Phys. Oceanogr.*, **27**, 555–566,  
827 [https://doi.org/10.1175/1520-0485\(1997\)027<0555:SCABEI>2.0.CO;2](https://doi.org/10.1175/1520-0485(1997)027<0555:SCABEI>2.0.CO;2).

828 Dai, L., H. Xie, S. F. Ackley, and A. M. Mestas-Nuñez, 2020: Ice Production in Ross Ice Shelf  
829 Polynyas during 2017–2018 from Sentinel-1 SAR Images. *Remote Sens.*, **12**, 1484,  
830 <https://doi.org/10.3390/rs12091484>.

831 Davis, A. M. J., and R. T. McNider, 1997: The Development of Antarctic Katabatic Winds and  
832 Implications for the Coastal Ocean. *J. Atmos. Sci.*, **54**, 1248–1261,  
833 [https://doi.org/10.1175/1520-0469\(1997\)054<1248:TDOAKW>2.0.CO;2](https://doi.org/10.1175/1520-0469(1997)054<1248:TDOAKW>2.0.CO;2).

834 Ding, Y., X. Cheng, X. Li, M. Shokr, J. Yuan, Q. Yang, and F. Hui, 2020: Specific Relationship  
835 between the Surface Air Temperature and the Area of the Terra Nova Bay Polynya, Antarctica.  
836 *Adv. Atmos. Sci.*, **37**, 532–544, <https://doi.org/10.1007/s00376-020-9146-2>.

837 Dong, S., J. Sprintall, S. T. Gille, and L. Talley, 2008: Southern Ocean mixed-layer depth from  
838 Argo float profiles. *J. Geophys. Res.*, **113**, C06013, <https://doi.org/10.1029/2006JC004051>.

839 Ekman, V. W., 1905: On the influence of the earth's rotation on ocean-currents. *Ark. För Mat.*  
840 *Astron. Och Fys.*, **2**, 1–53.

841 Guest, P. S., 2021a: Inside Katabatic Winds Over the Terra Nova Bay Polynya: 1. Atmospheric  
842 Jet and Surface Conditions. *J. Geophys. Res. Atmos.*, **126**,  
843 <https://doi.org/10.1029/2021JD034902>.

844 Guest, P. S., 2021b: Inside Katabatic Winds Over the Terra Nova Bay Polynya: 2. Dynamic and  
845 Thermodynamic Analyses. *J. Geophys. Res. Atmos.*, **126**,  
846 <https://doi.org/10.1029/2021JD034904>.

847 Hellmer, H. H., and D. J. Olbers, 1989: A two-dimensional model for the thermohaline circulation  
848 under an ice shelf. *Antarct. Sci.*, **1**, 325–336, <https://doi.org/10.1017/S0954102089000490>.

849 Hibler, W. D., 1979: A Dynamic Thermodynamic Sea Ice Model. *J. Phys. Oceanogr.*, **9**, 815–846,  
850 [https://doi.org/10.1175/1520-0485\(1979\)009<0815:ADTSIM>2.0.CO;2](https://doi.org/10.1175/1520-0485(1979)009<0815:ADTSIM>2.0.CO;2).

851 Jacobs, S. S., A. F. Amos, and P. M. Bruchhausen, 1970: Ross sea oceanography and antarctic  
852 bottom water formation. *Deep. Res. Oceanogr. Abstr.*, **17**, 935–962,  
853 [https://doi.org/10.1016/0011-7471\(70\)90046-X](https://doi.org/10.1016/0011-7471(70)90046-X).

854 Jenkins, A., H. H. Hellmer, and D. M. Holland, 2001: The Role of Meltwater Advection in the  
855 Formulation of Conservative Boundary Conditions at an Ice–Ocean Interface. *J. Phys.*  
856 *Oceanogr.*, **31**, 285–296, [https://doi.org/10.1175/1520-0485\(2001\)031<0285:TROMAI>2.0.CO;2](https://doi.org/10.1175/1520-0485(2001)031<0285:TROMAI>2.0.CO;2).

858 Kitade, Y., and Coauthors, 2014: Antarctic bottom water production from the Vincennes Bay  
859 Polynya, East Antarctica. *Geophys. Res. Lett.*, **41**, 3528–3534,  
860 <https://doi.org/10.1002/2014GL059971>.

861 Knuth, S. L., and J. J. Cassano, 2011: An analysis of near-surface winds, air temperature, and  
862 cyclone activity in Terra Nova Bay, Antarctica, from 1993 to 2009. *J. Appl. Meteorol.*  
863 *Climatol.*, **50**, 662–680, <https://doi.org/10.1175/2010JAMC2507.1>.

864 Kusahara, K., G. D. Williams, T. Tamura, R. Massom, and H. Hasumi, 2017: Dense shelf water  
865 spreading from Antarctic coastal polynyas to the deep Southern Ocean: A regional  
866 circumpolar model study. *J. Geophys. Res. Ocean.*, **122**, 6238–6253,  
867 <https://doi.org/10.1002/2017JC012911>.

868 Large, W. G., J. C. McWilliams, and S. C. Doney, 1994: Oceanic vertical mixing: A review and a  
869 model with a nonlocal boundary layer parameterization. *Rev. Geophys.*, **32**, 363–403,  
870 <https://doi.org/10.1029/94RG01872>.

871 Large, W. G., and S. G. Yeager, 2004: Diurnal to decadal global forcing for ocean and sea-ice  
872 models: The data sets and flux climatologies. (*Tech. Note TN-460+STR*), Boulder, CO:  
873 NCAR, <https://doi.org/10.5065/D6KK98Q6>.

874 Le Bel, D. A., C. J. Zappa, G. Budillon, and A. L. Gordon, 2021: Salinity response to atmospheric  
875 forcing of the Terra Nova Bay polynya, Antarctica. *Antarct. Sci.*, **14**, 1–14,  
876 <https://doi.org/10.1017/S0954102021000146>.

877 Lentz, S. J., 2008: Seasonal Variations in the Circulation over the Middle Atlantic Bight  
878 Continental Shelf. *J. Phys. Oceanogr.*, **38**, 1486–1500,  
879 <https://doi.org/10.1175/2007JPO3767.1>.

880 Li, Y., R. Ji, S. Jenouvrier, M. Jin, and J. Stroeve, 2016: Synchronicity between ice retreat and  
881 phytoplankton bloom in circum-Antarctic polynyas. *Geophys. Res. Lett.*, **43**, 2086–2093,  
882 <https://doi.org/10.1002/2016GL067937>.

883 Lipscomb, W. H., E. C. Hunke, W. Maslowski, and J. Jakacki, 2007: Ridging, strength, and  
884 stability in high-resolution sea ice models. *J. Geophys. Res. Ocean.*, **112**, 1–18,  
885 <https://doi.org/10.1029/2005JC003355>.

886 Losch, M., 2008: Modeling ice shelf cavities in a z coordinate ocean general circulation model. *J.  
887 Geophys. Res.*, **113**, C08043, <https://doi.org/10.1029/2007JC004368>.

888 Losch, M., D. Menemenlis, J. M. Campin, P. Heimbach, and C. Hill, 2010: On the formulation of  
889 sea-ice models. Part 1: Effects of different solver implementations and parameterizations.  
890 *Ocean Model.*, **33**, 129–144, <https://doi.org/10.1016/j.ocemod.2009.12.008>.

891 Marshall, J., A. Adcroft, C. Hill, L. Perelman, and C. Heisey, 1997: A finite-volume,  
892 incompressible navier stokes model for, studies of the ocean on parallel computers. *J.  
893 Geophys. Res. C Ocean.*, **102**, 5753–5766, <https://doi.org/10.1029/96JC02775>.

894 Martin, A., M. N. Houssais, H. Le Goff, C. Marec, and D. Dausse, 2017: Circulation and water  
895 mass transports on the East Antarctic shelf in the Mertz Glacier region. *Deep. Res. Part I  
896 Oceanogr. Res. Pap.*, **126**, 1–20, <https://doi.org/10.1016/j.dsr.2017.05.007>.

897 Martinson, D. G., and C. Wamser, 1990: Ice drift and momentum exchange in winter Antarctic  
898 pack ice. *J. Geophys. Res.*, **95**, 1741, <https://doi.org/10.1029/JC095iC02p01741>.

899 Mathiot, P., B. Barnier, H. Gallée, J. M. Molines, J. Le Sommer, M. Juza, and T. Penduff, 2010:  
900 Introducing katabatic winds in global ERA40 fields to simulate their impacts on the Southern  
901 Ocean and sea-ice. *Ocean Model.*, **35**, 146–160,  
902 <https://doi.org/10.1016/j.ocemod.2010.07.001>.

903 Mathiot, P., N. C. Jourdain, B. Barnier, H. Gallée, J. M. Molines, J. Le Sommer, and T. Penduff,  
904 2012: Sensitivity of coastal polynyas and high-salinity shelf water production in the Ross Sea,  
905 Antarctica, to the atmospheric forcing. *Ocean Dyn.*,

906 Meehl, G. A., J. M. Arblaster, C. T. Y. Chung, M. M. Holland, A. DuVivier, L. A. Thompson, D.  
907 Yang, and C. M. Bitz, 2019: Sustained ocean changes contributed to sudden Antarctic sea ice  
908 retreat in late 2016. *Nat. Commun.*, **10**, 1–9, <https://doi.org/10.1038/s41467-018-07865-9>.

909 Morales Maqueda, M. A., A. J. Willmott, and N. R. T. Biggs, 2004: Polynya Dynamics: a Review  
910 of Observations and Modeling. *Rev. Geophys.*, **42**, <https://doi.org/10.1029/2002RG000116>.

911 Nakayama, Y., M. Schröder, and H. H. Hellmer, 2013: From circumpolar deep water to the glacial  
912 meltwater plume on the eastern Amundsen Shelf. *Deep Sea Res. Part I Oceanogr. Res. Pap.*,  
913 **77**, 50–62, <https://doi.org/10.1016/j.dsr.2013.04.001>.

914 Nakayama, Y., D. Menemenlis, M. Schodlok, and E. Rignot, 2017: Amundsen and Bellingshausen  
915 Seas simulation with optimized ocean, sea ice, and thermodynamic ice shelf model  
916 parameters. *J. Geophys. Res. Ocean.*, **122**, 6180–6195,  
917 <https://doi.org/10.1002/2016JC012538>.

918 Nakayama, Y., and Coauthors, 2019: Pathways of ocean heat towards Pine Island and Thwaites  
919 grounding lines. *Sci. Rep.*, **9**, 1–9, <https://doi.org/10.1038/s41598-019-53190-6>.

920 Nguyen, A. T., D. Menemenlis, and R. Kwok, 2011: Arctic ice-ocean simulation with optimized  
921 model parameters: Approach and assessment. *J. Geophys. Res. Ocean.*, **116**, 1–18,  
922 <https://doi.org/10.1029/2010JC006573>.

923 Nihashi, S., and K. I. Ohshima, 2015: Circumpolar Mapping of Antarctic Coastal Polynyas and  
924 Landfast Sea Ice: Relationship and Variability. *J. Clim.*, **28**, 3650–3670,  
925 <https://doi.org/10.1175/JCLI-D-14-00369.1>.

926 Ohshima, K. I., and Coauthors, 2013: Antarctic Bottom Water production by intense sea-ice  
927 formation in the Cape Darnley polynya. *Nat. Geosci.*, **6**, 235–240,  
928 <https://doi.org/10.1038/ngeo1738>.

929 Ohshima, K. I., and Coauthors, 2022: Dominant frazil ice production in the Cape Darnley polynya  
930 leading to Antarctic Bottom Water formation. *Sci. Adv.*, **8**, 1–11,  
931 <https://doi.org/10.1126/sciadv.adc9174>.

932 Orlanski, I., 1976: A simple boundary condition for unbounded hyperbolic flows. *J. Comput. Phys.*,  
933 **21**, 251–269, [https://doi.org/10.1016/0021-9991\(76\)90023-1](https://doi.org/10.1016/0021-9991(76)90023-1).

934 Parish, T. R., and D. H. Bromwich, 2007: Reexamination of the near-surface airflow over the  
935 Antarctic continent and implications on atmospheric circulations at high southern latitudes.  
936 *Mon. Weather Rev.*, **135**, 1961–1973, <https://doi.org/10.1175/MWR3374.1>.

937 Parmiggiani, F., 2006: Fluctuations of Terra Nova Bay polynya as observed by active (ASAR) and  
938 passive (AMSR-E) microwave radiometers. *Int. J. Remote Sens.*, **27**, 2459–2467,  
939 <https://doi.org/10.1080/01431160600554355>.

940 Pease, C. H., 1987: The size of wind-driven coastal polynyas. *J. Geophys. Res. Ocean.*, **92**, 7049–  
941 7059, <https://doi.org/10.1029/JC092iC07p07049>.

942 Rocha, C. B., T. K. Chereskin, S. T. Gille, and D. Menemenlis, 2016: Mesoscale to submesoscale  
943 wavenumber spectra in Drake Passage. *J. Phys. Oceanogr.*, **46**, 601–620,  
944 <https://doi.org/10.1175/JPO-D-15-0087.1>.

945 Roquet, F., and Coauthors, 2021: MEOP-CTD in-situ data collection: a Southern ocean Marine-  
946 mammals calibrated sea water temperatures and salinities observations. *SEANOE*,  
947 <https://doi.org/10.17882/45461>.

948 Roquet, F., and Coauthors, 2014: A Southern Indian Ocean database of hydrographic profiles  
949 obtained with instrumented elephant seals. *Sci. Data*, **1**, 140028,  
950 <https://doi.org/10.1038/sdata.2014.28>.

951 Rusciano, E., G. Budillon, G. Fusco, and G. Spezie, 2013: Evidence of atmosphere-sea ice-ocean  
952 coupling in the Terra Nova Bay polynya (Ross Sea-Antarctica). *Cont. Shelf Res.*, **61–62**, 112–  
953 124, <https://doi.org/10.1016/j.csr.2013.04.002>.

954 Schmidtko, S., K. J. Heywood, A. F. Thompson, and S. Aoki, 2014: Multidecadal warming of  
955 Antarctic waters. *Science*, **346**, 1227–1231, <https://doi.org/10.1126/science.1256117>.

956 Schultz, C., S. C. Doney, W. G. Zhang, H. Regan, P. Holland, M. P. Meredith, and S. Stammerjohn,  
957 2020: Modeling of the Influence of Sea Ice Cycle and Langmuir Circulation on the Upper  
958 Ocean Mixed Layer Depth and Freshwater Distribution at the West Antarctic Peninsula. *J.  
959 Geophys. Res. Ocean.*, **125**, <https://doi.org/10.1029/2020JC016109>.

960 Silvano, A., S. R. Rintoul, B. Peña-Molino, W. R. Hobbs, E. Van Wijk, S. Aoki, T. Tamura, and  
961 G. D. Williams, 2018: Freshening by glacial meltwater enhances melting of ice shelves and  
962 reduces formation of Antarctic Bottom Water. *Sci. Adv.*, **4**,  
963 <https://doi.org/10.1126/sciadv.aap9467>.

964 Smagorinsky, J., 1963: General Circulation Experiments With the Primitive Equations. *Mon.  
965 Weather Rev.*, **91**, 99–164, [https://doi.org/10.1175/1520-  
966 0493\(1963\)091<0099:gcewtp>2.3.co;2](https://doi.org/10.1175/1520-0493(1963)091<0099:gcewtp>2.3.co;2).

967 Smith, W. O., Jr., and D. G. Barber, Eds., 2007: *Polynyas: Windows to the World*. Elsevier Science,  
968 474 pp.

969 Snow, K., B. M. Sloyan, S. R. Rintoul, A. M. Hogg, and S. M. Downes, 2016: Controls on  
970 circulation, cross-shelf exchange, and dense water formation in an Antarctic polynya.  
971 *Geophys. Res. Lett.*, **43**, 7089–7096, <https://doi.org/10.1002/2016GL069479>.

972 Stewart, A. L., A. Klocker, and D. Menemenlis, 2019: Acceleration and Overturning of the  
973 Antarctic Slope Current by Winds, Eddies, and Tides. *J. Phys. Oceanogr.*, **49**, 2043–2074,  
974 <https://doi.org/10.1175/JPO-D-18-0221.1>.

975 St-Laurent, P., J. M. Klinck, and M. S. Dinniman, 2013: On the role of coastal troughs in the  
976 circulation of warm circumpolar deep water on Antarctic shelves. *J. Phys. Oceanogr.*, **43**,  
977 51–64, <https://doi.org/10.1175/JPO-D-11-0237.1>.

978 Tamura, T., K. I. Ohshima, and S. Nihashi, 2008: Mapping of sea ice production for Antarctic  
979 coastal polynyas. *Geophys. Res. Lett.*, **35**, 1–5, <https://doi.org/10.1029/2007GL032903>.

980 Tamura, T., K. I. Ohshima, A. D. Fraser, and G. D. Williams, 2016: Sea ice production variability  
981 in Antarctic coastal polynyas. *J. Geophys. Res. Ocean.*, **121**, 2967–2979,  
982 <https://doi.org/10.1002/2015JC011537>.

983 Thorndike, A. S., D. A. Rothrock, G. A. Maykut, and R. Colony, 1975: The thickness distribution  
984 of sea ice. *J. Geophys. Res.*, **80**, 4501–4513, <https://doi.org/10.1029/jc080i033p04501>.

985 Tison, J.-L., and Coauthors, 2020: Physical and biological properties of early winter Antarctic sea  
986 ice in the Ross Sea. *Ann. Glaciol.*, **61**, 241–259, <https://doi.org/10.1017/aog.2020.43>.

987 Turner, J. S., 1973: *Buoyancy Effects in Fluids*. Cambridge University Press, 367 pp.

988 Van Woert, M. L., 1999: Wintertime dynamics of the Terra Nova Bay polynya. *J. Geophys. Res.*  
989 *Ocean.*, **104**, 7753–7769, <https://doi.org/10.1029/1999jc900003>.

990 Visbeck, M., J. Marshall, and H. Jones, 1996: Dynamics of isolated convective regions in the ocean.  
991 *J. Phys. Oceanogr.*, **26**, 1721–1734, [https://doi.org/10.1175/1520-0485\(1996\)026<1721:DOICRI>2.0.CO;2](https://doi.org/10.1175/1520-0485(1996)026<1721:DOICRI>2.0.CO;2).

993 Wendler, G., D. Gilmore, and J. Curtis, 1997: On the formation of coastal polynyas in the area of  
994 Commonwealth Bay, Eastern Antarctica. *Atmos. Res.*, **45**, 55–75,  
995 [https://doi.org/10.1016/S0169-8095\(97\)00024-0](https://doi.org/10.1016/S0169-8095(97)00024-0).

996 Wenta, M., and J. J. Cassano, 2020: The Atmospheric Boundary Layer and Surface Conditions  
997 during Katabatic Wind Events over the Terra Nova Bay Polynya. *Remote Sens.*, **12**, 4160,  
998 <https://doi.org/10.3390/rs12244160>.

999 Wilchinsky, A. V., and D. L. Feltham, 2008: Generation of a Buoyancy-Driven Coastal Current  
1000 by an Antarctic Polynya. *J. Phys. Oceanogr.*, **38**, 1011–1032,  
1001 <https://doi.org/10.1175/2007JPO3831.1>.

1002 Williams, G. D., S. Aoki, S. S. Jacobs, S. R. Rintoul, T. Tamura, and N. L. Bindoff, 2010: Antarctic  
1003 bottom water from the adélie and George v Land Coast, East Antarctica (140-149°E). *J.*  
1004 *Geophys. Res. Ocean.*, **115**, 1–29, <https://doi.org/10.1029/2009JC005812>.

1005 Williams, G. D., and N. L. Bindoff, 2003: Wintertime oceanography of the Adélie Depression.  
1006 *Deep. Res. Part II Top. Stud. Oceanogr.*, **50**, 1373–1392, [https://doi.org/10.1016/S0967-0645\(03\)00074-2](https://doi.org/10.1016/S0967-0645(03)00074-2).

1008 Williams, G. D., N. L. Bindoff, S. J. Marsland, and S. R. Rintoul, 2008: Formation and export of  
1009 dense shelf water from the Adélie depression, East Antarctica. *J. Geophys. Res. Ocean.*, **113**,  
1010 1–12, <https://doi.org/10.1029/2007JC004346>.

1011 Winsor, P., and G. Björk, 2000: Polynya activity in the Arctic Ocean from 1958 to 1997. *J.  
1012 Geophys. Res. Ocean.*, **105**, 8789–8803, <https://doi.org/10.1029/1999jc900305>.

1013 Xu, Y., W. G. Zhang, T. Maksym, R. Ji, and Y. Li, 2023: Stratification Breakdown in Antarctic  
1014 Coastal Polynyas, Part II: Influence of an Ice Tongue and Coastline Geometry, submitted.

1015 Zhang, J., and W. D. Hibler, 1997: On an efficient numerical method for modeling sea ice  
1016 dynamics. *J. Geophys. Res. Ocean.*, **102**, 8691–8702, <https://doi.org/10.1029/96JC03744>.

1017 Zhang, W. G., and C. Cenedese, 2014: The dispersal of dense water formed in an idealized coastal  
1018 polynya on a shallow sloping shelf. *J. Phys. Oceanogr.*, **44**, 1563–1581,  
1019 <https://doi.org/10.1175/JPO-D-13-0188.1>.

1020